

Light-Curve and Spectral Properties of Type II Supernovae from the ATLAS survey

K. Ertini^{1,2}, J. P. Anderson³, G. Folatelli^{1,2,4}, S. González-Gaitán^{5,3}, C. P. Gutiérrez^{6,7}, J. Sollerman⁸, O. Rodríguez^{9,10}, A. Aryan¹¹, T.-W. Chen¹¹, E. Concepcion¹², S.P. Cosentino¹³, M. Dennefeld¹⁴, N. Erasmus^{15,16}, M. Fraser¹⁷, L. Galbany^{6,7}, M. Gromadzki¹⁸, C. Inserra¹⁹, T. E. Müller-Bravo^{20,21}, P. J. Pessi^{8,22}, T. Pessi³, T. Petrushevska¹², G. Pignata²³, F. Ragosta^{24,25}, S. Srivastav²⁶, and D. R. Young²⁷

(Affiliations can be found after the references)

Received XXX; accepted XXX

ABSTRACT

Context. Type II supernovae (SNe) are the most common terminal stellar explosions in the Universe. With SNe now being detected within days after explosion, there is growing evidence that the majority of Type II SNe (SNe II) show signs of interaction with a confined, dense circumstellar material (CSM) in the first few days post explosion.

Aims. In this work we aim to bridge the gap between single SN studies showing early-time interaction in their spectra, and the statistical studies of early-time SN light curves, which imply the existence of CSM.

Methods. We present a sample of 68 Type II SNe with both early photometric data, obtained with the ATLAS survey, and spectroscopic data, obtained with the ePESSTO+ collaboration. A subset of the sample is classified based on the presence or absence of narrow spectral features with electron-scattered broadened wings in the early spectra, indicative of interaction with CSM. We characterise the photometric and spectroscopic properties of the sample by measuring rise times to maximum light, peak magnitudes, decline rates and line velocities. Additionally, we measure the ratio of absorption to emission (a/e) of the H α P-Cygni profile.

Results. Our analysis reveals that SNe II showing early spectroscopic signs of interaction with CSM decline faster and are brighter than those without. However no difference is found in rise times between the two groups. A clear separation is observed in the a/e ratio: SNe with signs of interaction exhibit lower a/e ratios at all epochs compared to those without. Our results highlight that understanding SN II ejecta-CSM interaction requires large, uniform samples of photometric and spectroscopic data, such as the one presented in this work.

Key words. supernovae:general – stars:massive

1. Introduction

Type II supernovae (SNe II) are the most abundant terminal explosions, arising from stars more massive than $\approx 8 M_{\odot}$ (Li et al. 2011; Shivers et al. 2017), which have retained their hydrogen envelopes. Direct detection of progenitor stars has established conclusive evidence that these SNe arise from red supergiant (RSG) stars (e.g. Maund et al. 2005; Fraser et al. 2012; Van Dyk et al. 2012; Smartt 2015; Kilpatrick et al. 2023). A subclass of SNe II are Type IIn, which show narrow emission lines in their spectra. Such narrow emission lines are thought to result from the collision between the SN ejecta and slow-moving dense circumstellar material (CSM) near the progenitor star (Schlegel 1990). Until recently, it was believed that ‘normal’ SNe II explode in relatively clean environments, where any interaction between the SN ejecta and their environment had negligible effect on the observed transient. However, this picture has changed during the past decade.

In recent years, there has been an increasing number of early-time observations of SNe II, within days or even hours after the explosion. Several surveys now focus on discovering transients with high cadence, providing such early-time observations. Observations of some SNe II within hours to a few days post-explosion reveal spectra dominated by narrow, highly ionized emission lines with electron-scattered wings (also called “flash features”), implying strong interaction with a dense, slow-moving CSM (e.g. Niemela et al. 1985; Leonard et al. 2000;

Yaron et al. 2017). However, in contrast to SNe IIn, these features then gradually disappear on timescales of hours to days, and spectra transform to those of “normal” SNe II. Sample studies centered on these high ionization features can be found in Khazov et al. (2016), Bruch et al. (2021), Bruch et al. (2023), and Jacobson-Galán et al. (2024).

In the last years, the discovery of two nearby SNe II made it possible to constrain CSM properties with significant precision. SN 2023ixf and SN 2024ggi were discovered by Itagaki (2023) and Srivastav et al. (2024), respectively, and they were both located at ~ 7 Mpc. Their early detection enabled a detailed tracking of the flash features, allowing estimations of their mass-loss (\dot{M}) histories and progenitor properties, and providing constraints on late-time stellar evolution and progenitor density profiles. Another relevant example is SN 2021yja, which was detected only ≈ 5 hours after explosion (Smith et al. 2021). Unlike SN 2023ixf and SN 2024ggi, it did not exhibit flash features in its early spectra. However, it did show broader features and a particular “ledge-shaped” feature around 450–480 nm, which has been interpreted as a possible sign of interaction with a low mass CSM (Hosseinzadeh et al. 2022; Soumagnac et al. 2020). These cases highlight the diversity in early-time spectroscopic signatures among SNe II and also how the varying degrees of CSM interaction can shape early-time transient evolution.

SN-II spectra during the plateau phase also exhibit signs of interaction with CSM. For instance, Faran et al. (2014) analysed a sample of 23 SNe and identified potential evidence of CSM

interaction in the spectra of at least six events. These SNe displayed high-velocity features in the blue wing of $H\alpha$ during the plateau phase, with a similar behaviour observed in $H\beta$. Subsequently, Gutiérrez et al. (2017a) conducted a comprehensive study of over 100 SNe II and reported further potential indications of CSM interaction in a significant fraction of the sample during the recombination phase.

The early rise of SN II light curves (LCs) can provide constraints on the progenitor and its environment. In a clean environment, the properties of the LC during the early radiation-dominated phase primarily depend on the progenitor radius, explosion energy, and progenitor mass. When the CSM is considered, the influence of the progenitor properties on the early LC diminishes, whereas the properties of the CSM have a significant effect (Moriya et al. 2011; Dessart et al. 2017; Dessart & Jacobson-Galán 2023; Cosentino et al. 2025). Sample studies using observations of SNe II focusing on the early behaviour elucidate the observation of this effect. The rise times in observed broad-band LCs are found to be short relative to what is expected in clean RSG progenitor explosions. This discrepancy was first identified observationally by Gall et al. (2015) and González-Gaitán et al. (2015) and later by Rubin et al. (2016) and Bruch et al. (2023). However, these rise times are long compared with the expected shock breakout (SBO) from the stellar surface. González-Gaitán et al. (2015) attributed the short rise times either to the shock cooling caused by the core collapse of a RSG with compact and dense envelopes, or to the delayed SBO following the collapse of a RSG with an extended atmosphere or pre-SN CSM. By analyzing a sample of 26 SNe II, Förster et al. (2018) argued that the observed emission is consistent with the SBO through a dense CSM rather than directly from the stellar surface. This finding suggests that the characteristic hour-long SBO timescales expected from stellar envelopes may be rare in nature. Instead, in most SNe II, the SBO could be delayed due to the presence of significant CSM.

In the last decade, modelling efforts have been made to understand the early behaviour of both LCs and spectra of SNe II, and to understand how they are affected by CSM interaction. Studies that modelled RSG star explosions embedded in a variety of dense envelopes showed that the early luminosity, color evolution, and photospheric velocities are strongly affected by the properties of the CSM and that if the CSM is dense enough, the SBO is delayed (Moriya et al. 2011; Morozova et al. 2017; Dessart et al. 2017). When comparing some of these models with observations of SNe II with early interaction (i.e. those showing flash ionization lines), usually high mass loss rates are required $\dot{M} \sim 10^{-3} - 10^{-2} M_{\odot} \text{ yr}^{-1}$, while what is observed in RSG is on the order of $\dot{M} \sim 10^{-6} M_{\odot} \text{ yr}^{-1}$ (Beasor & Davies 2018). However, when taking the RSG wind acceleration into account, even if the mass-loss rate of the progenitor is relatively low it can produce a dense CSM at the immediate stellar vicinity and the early LCs of SNe II can be significantly affected (Moriya et al. 2018, 2023).

Discrepancies arise when comparing what is expected from standard stellar evolution theory with the observations of SNe II with early interaction. While models predict that the luminosity and color evolution should be strongly influenced by the properties of the CSM at early times, Bruch et al. (2023) argued that SNe II showing flash features are not significantly brighter, nor bluer, nor more slowly rising than those without. They suggest that the CSM creating the flash features is not massive enough to contribute significantly to the luminosity of SNe II. On the contrary, Jacobson-Galán et al. (2024) and Jacobson-Galán et al. (2025) recently reported that SNe II with early interaction do

appear to be bluer and more luminous. These inconsistencies could be due to how the samples are constructed and classified based on flash spectroscopy, but they highlight the ongoing uncertainty regarding how RSG progenitors generate the required dense CSM and how this affects the observed properties of SNe II.

The objective of this work is to combine the detailed spectroscopic analysis of individual events with large-scale statistical LC analysis to further understand the frequency and effects of early interaction on the properties of SNe II. In this study, we present an early-time photometric analysis of a large SN II sample. This is complemented by a large set of spectroscopic data obtained from early times to plateau epochs.

This paper is organised as follows: in Section 2 we present the sample, including the LCs and spectra. In Section 3 we outline the methods employed for the photometric and spectral measurements. Section 4 presents the correlations between parameters and in Section 5 we discuss our results.

2. Data sample

The SN II sample was compiled between 2019 and 2023 making use of the Asteroid Terrestrial-impact Last Alert System (ATLAS; Tonry et al. 2018; Smith et al. 2020) for the photometry, and of the Public European Southern Observatory Spectroscopic Survey of Transient Objects (ePESSTO+) collaboration (Smartt et al. 2015) for the spectral data. SNe were selected based on the following criteria: 1) being classified as a SN II, 2) having ATLAS photometry, 3) having a constraining non-detection less than four days before the first detection, 4) being brighter than 18th mag at optical wavelengths at maximum light, and 5) being observable from La Silla Observatory and continue to be for the next few months. Taking these criteria into account, we collected data from 77 SNe. We excluded Type IIn and IIb SNe.

We downloaded the photometry from the ATLAS forced photometry server¹. The measurements from the photometry server come from a PSF fitting routine, based on algorithms from Tonry (2011) and Sonnett et al. (2013). The output gives the MJD of the start of the exposure, the AB magnitude, the flux, and the reduced χ^2 of the PSF fit, among other parameters. Photometry is obtained in the c (wavelength range 4200–6500 Å) and o (5600–8200 Å) ATLAS passbands. An example of a light curve of a SN in our sample is shown in Figure 1.

Once a SN was selected to be a part of the sample, spectra were obtained with the ESO Faint Object Spectrograph and Camera (EFOSC2; Buzzoni et al. 1984) mounted on the NTT at La Silla Observatory. Our primary choice was to perform the observations with grism #13, which covers a wavelength range of 3685–9315 Å and has a resolution of 21.2 Å. Occasionally, we used grisms #11 and #16, which cover ranges of 3380–7520 Å and 6015–10320 Å, with resolutions of 15.8 and 16.0 Å, respectively. We typically used a 1".0 slit, but in bad seeing conditions a 1".5 slit was adopted. The integration times varied between 1500 and 3600 s. All spectra were reduced following standard procedures using the ePESSTO+² pipeline. We collected a total of 194 spectra. In some SNe the Type II classification was unclear (even if such a classification had been initially reported) due to non-standard features in their spectra. In these cases we re-classified the events using the Supernova Identification code (SNID; Blondin & Tonry 2007). We reclassified eight SNe. Five were reclassified as Type IIb: SN 2019sox,

¹ <https://fallingstar-data.com/forcedphot/>

² <https://github.com/svalenti/pessto>

Table 1: Initial sample size and its reduction in each step of our analysis.

Photometric sample			
Step	Criteria	Removed	Objects left
1	Initial sample	–	77
2	Re-classification	9	68
3	No deep non-detection	4	64
Spectroscopic sample			
Step	Criteria	Removed	Objects left
1	Initial sample	–	54
2	Only photospheric spectra	9	45
3	Measurable H β	24	21

SN 2019tua, SN 2020utf, SN 2021fox, and SN 2022aczs; two Type Ia: SN 2020skx and SN 2022yeg; and one Type IIn, SN 2020ntl. We removed these SNe from our sample, but their photometry and spectral sequences will be made available via Zenodo³. Also, we note that the spectra of SN 2020uwl do not show any typical P-Cygni feature, which led us to believe that this is a peculiar event, hence we removed it from the sample, but we show its photometric and spectral behaviour in Zenodo. We identified four SNe which have an SN 1987A-like light curve behaviour: SN 2021aatt, SN 2021adcw, SN 2021adyl and SN 2022acrv. While such SNe are clearly different from ‘normal’ SNe II, we kept them in our sample to highlight their properties, but removed them/treat them differently in some specific analysis/correlations presented below.

Among the remaining 68 SNe II, there were 14 where we could not obtain any spectra. We kept these SNe as part of the sample, and we included them in all the photometric calculations, but they were not included in the spectral measurements. While we were unable to obtain any spectra with EFOSC2, each of these SNe have a classification spectrum, so we are certain they are Type IIs. Additionally, to ensure there were no bias in the selection of objects, we checked if the magnitudes of the 14 SNe for which we did not get spectra were particularly sub-luminous. We found that 13/14 SNe fall within the mean M_{max} (see Section 4.1) and only one SN is sub-luminous, so we consider this not to be a bias. An example of a spectral sequence of an SN of our sample is shown in Figure 2.

The 68 selected SNe are listed in Table A.1, along with their host galaxy information, and discovery date. Additionally, in Table 1 the selection steps are listed.

3. Light-curve and spectral measurements

Using o - and c -band photometry for 68 SNe II, along with optical-wavelength spectroscopy for a subset of 54 SNe within that initial sample, this study aims to investigate the LC and spectral properties of a statistically significant sample of SNe II with early-time photometric data. These data are then used to constrain the progenitor and explosion properties of SNe II, and more importantly to assess the presence and effect of any significant CSM material surrounding the progenitor stars at the time of explosion.

Following the above goals, in the below subsections we define our LC and spectral measurements to be used in characterising this SN II sample. First, we present our first-light epoch estimation method and then outline the adopted distances and Milky-Way line-of-sight extinction (host-galaxy extinction is ig-

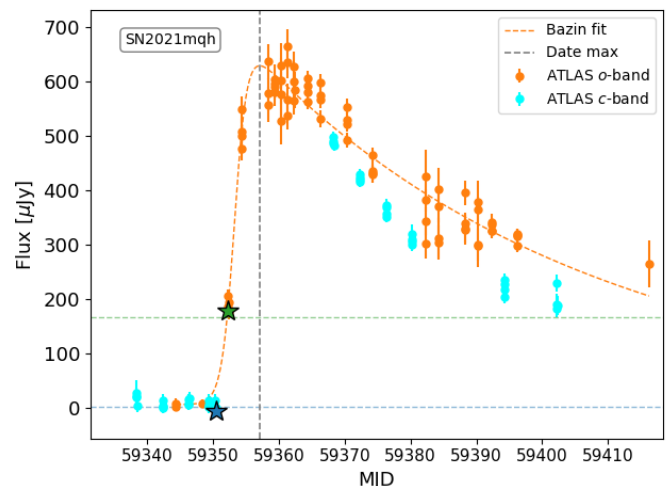


Fig. 1: Example of LC of a SN II from our sample. The weighted average detection epoch and last non-detection are marked as green and blue stars, respectively. Dashed horizontal lines indicate the flux levels of the last non-detection plus one sigma uncertainty (blue line) and of the first detection minus one sigma uncertainty (green line). If the difference between the two dashed lines is > 0 , we consider the non detection to be deep enough. The orange dashed line corresponds to the Bazin fit performed on the o -band LC (see Section 3.4.2), and the dashed vertical gray line shows the time of maximum light based on the fit.

nored, see our justification in Section 3.3). Then we define our light-curve measurements: absolute peak magnitudes, rise times to maximum light, and post-peak decline rates. Lastly, we define our spectral measurements: expansion velocities and the “bluest expansion velocity” (highest velocity at which we can measure a blue-shifted absorption) for H α , H β , and Fe II $\lambda 5169$.

3.1. First-light epoch estimations

Our initial sample was constructed by considering SNe II with published non-detections on the Transient Name Server (TNS⁴) occurring at most four days before the first detection. However, in some cases these published values (that are often automatically sent to the TNS) are not particularly constraining for the first-light epoch, for example when the “non-detection” provides an upper limit that is actually brighter than the discovery photometry. Therefore, we re-analysed our full sample to robustly define the non-detection and first detection and thus the estimated first-light epoch. We only used ATLAS forced photometry values for non-detections and detections to maintain consistency and avoid any potential systematic effects from information from other surveys that have different sensitivity and cadence. This was the approach even when the discovery of a SN was first reported by another survey. Since ATLAS obtains four points per epoch bin, we calculated the weighted average of the flux measurements in each bin corresponding to the detection epoch (MJD_{disc}) to obtain the detection flux. To determine the last deep non detection, we also calculated the weighted average of the flux measurements per epoch prior to the reported detection epoch. For both detection and non-detection we inferred the weighted standard deviation based on the individual measurement uncertainties. We considered the flux prior to detection to

³ <https://zenodo.org/>

⁴ <https://www.wis-tns.org/>

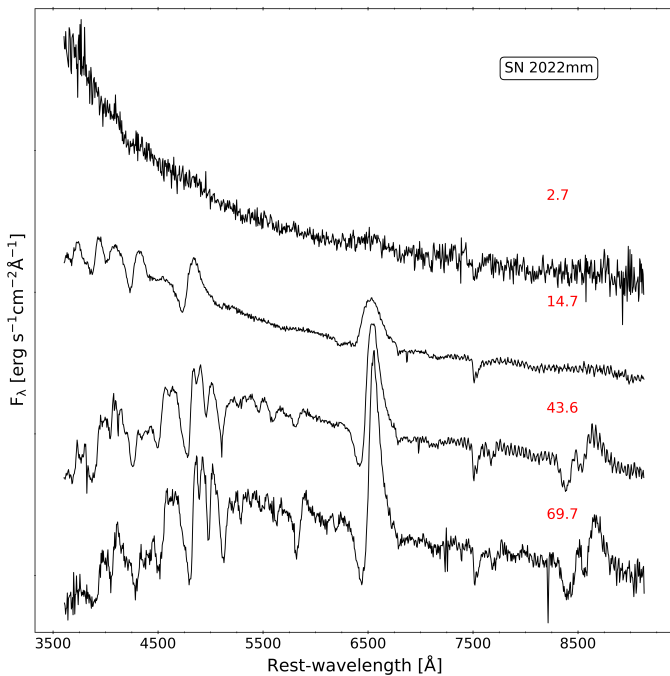


Fig. 2: Example of spectral sequence for SN 2022mm. The phase in days from first light is indicated in red next to each spectrum.

be deep enough for a non-detection if: 1) the forced photometry value was consistent with zero flux within one sigma, and 2) the error bars of the detection and non-detection did not overlap. When these two conditions were met, we adopted these as the last non-detection epoch ($MJD_{\text{non-det}}$) and first detection epoch. An example of this method is shown in Figure 1.

For approximately 10 % of the sample, we found that the errors overlapped or that the flux at non-detection was not consistent with zero. In those cases, we used the previous forced photometry value before the original non-detection or the next flux value after the detection, depending on the situation, and iterated the process. As our sample was constructed to ensure a deep non-detection less than four days before the detection, we verified that this condition was still met. For four SNe, SN 2020uwl, SN 2021dbg, SN 2022cvu, and SN 2022fli, this was not satisfied. To maintain consistency, we removed these SNe from our sample. The first-light epochs for all the SNe were then calculated as the midpoint between the SN discovery date and the non-detection. The uncertainty associated with this epoch was taken as $(MJD_{\text{disc}} - MJD_{\text{non-det}})/2$.

3.2. Distance estimations

The distances for the SNe II are based on redshift when the recession velocity is larger than 2000 km s^{-1} . To calculate the luminosity distances, we used the following approximation:

$$d_L = \frac{(1+z_{\text{helio}})}{(1+z_{\text{CMB}})} \frac{c}{H_0} \times \left[z_{\text{CMB}} + \frac{1}{2} \left(\Omega_\Lambda - \frac{\Omega_M}{2} + 1 \right) + z_{\text{CMB}}^2 \right], \quad (1)$$

where z_{helio} is the heliocentric redshift of the host galaxy, z_{CMB} is the redshift referred to the CMB rest frame, and H_0 and Ω_M are set to $H_0 = 67.4 \pm 0.5 \text{ km s}^{-1} \text{ Mpc}^{-1}$ and $\Omega_M = 0.315 \pm 0.007$, respectively (Planck Collaboration et al. 2020). The factor $(1+z_{\text{helio}})/(1+z_{\text{CMB}})$ accounts for the fact that the

photon redshift is observed with respect to the heliocentric reference system. The heliocentric redshift was calculated from the measurements of narrow emission lines originating from the host H II regions within the SN spectrum, then the z_{CMB} was obtained from the NASA Extragalactic Database (NED⁵) velocity correction calculator. We estimated the redshift error (and propagated this to our distance error) considering: 1) the standard deviation of our measurements, and 2) the spectral resolution. A typical $\sigma_{z_{\text{helio}}} = 0.003$ was obtained. If we could not extract the H II regions either because the spectrum was noisy or because the galaxy was faint, we used the host galaxy redshift from NED, and the error reported there. If a host galaxy had recession velocities less than 2000 km s^{-1} , then a redshift-independent distance was taken from NED if available. This was the case for only one SN in the sample, SN 2021yja. For those SNe for which we could not resolve H II regions and their host galaxies did not have NED information, we used a redshift value obtained from spectral matching with SNID, and employed the inferred distance. In those cases we took the fit error that comes from SNID, with typical values of $\sigma_z = 0.003 - 0.01$.

Following the above procedure, there were 20 SNe for which we could estimate the redshift from H II regions, 37 SNe where we got the redshift from NED, 12 SNe for which the redshift was estimated by spectral matching, and 1 SN for which we used a redshift-independent distance. The mean redshift value of the sample is 0.023 and the median is 0.021.

3.3. Extinction

To correct for the line of sight extinction produced through absorption by intervening dust in the Milky Way, we take the E(B-V) from the Schlafly & Finkbeiner (2011) recalibration of the Schlegel et al. (1998) infrared-based dust map, available from NED, and together with an extinction law from Fitzpatrick (1999), with $R_V = 3.1$ we obtain A_V . To convert A_V values to the ATLAS bands we used the Python module *extinction*⁶.

We do not correct for host-galaxy extinction. Several methods exist in the literature to estimate host extinction. These include the Na I D equivalent width (Turatto et al. 2003; Rodríguez et al. 2023), the diffuse interstellar band (DIB) at 5780 Å (Phillips et al. 2013), the (V-I) colour excess at the end of the plateau (Olivares E. et al. 2010), the colour-colour curve method (Rodríguez et al. 2014, 2019), and the Balmer decrement (e.g. Domínguez et al. 2013). However, there are major caveats with all of these methods. In this sample, we have low-resolution optical spectra for a subset of SNe, but the Na I absorption in low-resolution spectra has been shown to be a bad proxy for measuring the extinction (Poznanski et al. 2011; Phillips et al. 2013). Additionally, the DIB relation requires moderate resolution and high signal-to-noise ratio spectra (Phillips et al. 2013), but such observations are lacking in our sample. From optical spectra one could measure the Balmer decrement but, it is unclear whether the SN exploded behind, in front of, or within the H II region. Concerning optical colours, our sample lacks extensive colour information. Even if we had more data, these methods assume that all SNe II share the same intrinsic colour at some epoch. However, de Jaeger et al. (2018) argued against such a simplistic scenario in an in-depth study of SN II colours. Furthermore, Faran et al. (2014) analyzed a sample of SNe II and concluded that no extinction correction method significantly improved the uniformity of the sample. This finding was supported by Gutiér-

⁵ <https://ned.ipac.caltech.edu/>

⁶ <https://extinction.readthedocs.io/en/latest/>

rez et al. (2017b), who discovered that stronger correlations (between various SN observables) within a SN II sample were obtained before applying any extinction corrections. Therefore, we decided to not correct for host extinction since any such corrections are likely to simply add noise to our results. However, we note that this is a caveat in our work.

3.4. Photometric properties

3.4.1. ATLAS *c*- and *o*-band photometry

After obtaining all ATLAS forced photometry for our sample as outlined in Section 2, we filtered the LCs by flux error, removing data with errors larger than $50 \mu\text{Jy}$ to remove spurious data points. Then, our analysis goal was to have robust rise-time estimations. To achieve this, we required sufficiently well-sampled LCs during the rise to maximum. Given the fast rise of SNe II, we defined this criterion to be at least one photometric epoch between first light and maximum. While the LCs in the *o*-band are typically well-sampled, those in the *c*-band often lack photometric points during the rise. We calculated the photometric parameters (as outlined below) for the entire sample in the *o*-band, and for 21 events in the *c*-band, which were the only SNe that had data during the rising phase. Since ATLAS *o*-band light-curves are rather noisy (photometric data points taken on the same night have large dispersion), after filtering by error, we still had substantial dispersion and a number of clear outliers. We thus decided to perform sigma-clipping on the LCs. Given the intrinsic variability in the data around maximum, we did not sigma-clip the values during the early, rapidly rising phase of the LC, from the time of first light to maximum light, to prevent losing useful data in the process; clipping was performed at epochs later than 10 days after first light. We used this 10-day limit because it is in agreement with the mean rise times found in previous works (see for example González-Gaitán et al. 2015, Gall et al. 2015, Pessi et al. 2019). We median sigma-clipped the values using a 4σ limit and a rolling window of 20 points. This is the range where the median distribution is calculated, which corresponds approximately to five days. *c*-band photometry displays less dispersion than the *o*-band photometry, so we did not perform sigma-clipping.

3.4.2. ATLAS SNe II light-curve measurements

We calculated the time of maximum light for our sample of SNe II by fitting the Bazin function (Bazin et al. 2009) to the LCs. This is a phenomenological function that has the form:

$$f(t) = A \frac{e^{-(t-t_0)/\tau_{\text{fall}}}}{1 + e^{(t-t_0)/\tau_{\text{rise}}}} + B, \quad (2)$$

where τ_{rise} , τ_{fall} , t_0 , A and B are treated as free parameters. τ_{rise} and τ_{fall} are related to the rise and fall of the LC, A and B are normalization and scaling factors, respectively, and t_0 is the inflection point for the function. The date of maximum light (t_{max}) can be calculated by taking the derivative of this function, as explained in González-Gaitán et al. (2015). The fits were calculated using Markov chain Monte Carlo (MCMC) methods with the python emcee package (Foreman-Mackey et al. 2013). This approach involves computing the posterior probability of the parameters given the observations, based on assumed prior distributions. The prior distributions were constructed by first performing a single fit for each SN using the python package SciPy to obtain initial best-fit parameters. Distributions for each parameter were then centered on these initial values. We employed

100 walkers and 10000 steps per walker, together with a burn-in period of 2000 steps. Next, the date of maximum light was computed taking the derivative of the Bazin function. We obtained a t_{max} value for each MCMC realization and then computed the mean and standard deviation. The rise times ($t_{\text{rise},c}$ and $t_{\text{rise},o}$) are then calculated as the difference between t_{max} and the time of first light. The uncertainty in the rise time is the result of adding the uncertainty in the first-light calculation and the uncertainties in the time of maximum in quadrature. We note that some SNe show two peaks in their LCs, they are: SN 2021tyw, SN 2021aatd (87A-like), SN 2022acko, and SN 2022acrv (87A-like). In those cases, we only fitted the first peak with the Bazin function.

Maximum-light absolute magnitudes ($M_{\text{max},c}$ and $M_{\text{max},o}$) were calculated using the distances and extinctions defined in Sections 3.2 and 3.3, respectively, and the apparent magnitudes at t_{max} . The uncertainty in the absolute magnitude at maximum is the result of adding in quadrature the uncertainty in the maximum flux calculation and the error in the distance.

For the decline rates, we adopted the definitions provided in Anderson et al. (2014), where s_1 represents the decline rate of the initial, steeper slope of the LC, and s_2 corresponds to the decline rate of the second, shallower slope in the LC. It is important to note that while Anderson et al. (2014) express these values in magnitudes per 100 days, we calculate them as the change in flux normalized to maximum per 100 days. We call it $\Delta f / 100$ days. We first normalized the LCs to their maximum flux. Then, piecewise linear fits were applied to the photometry, testing both single- and two-slope models to assess whether the LCs exhibit different evolutionary phases or follow a single trend. The fitting range extended from the time of maximum light to either the point where the LC becomes noise-dominated (we visually inspect the LCs to determine when this happens) or the end of the plateau phase, whichever occurred first. Then we used the Bayesian information criteria (BIC) to determine which fit was better. If the BIC favored one slope, then we considered $s_1=s_2$, while if the BIC favored two slopes, we considered two different values for s_1 and s_2 . The uncertainties on the decline rates were estimated from the fit error. The fits to the LCs are shown in Appendix B. For those SNe with two peaks in their LCs, again we only considered the first peak.

3.5. Spectral measurements

A focus of our work is to study how any possibly-present CSM affecting the early photometric SN II properties could also affect spectral properties observed at later times. In this work, we define early spectra as those obtained at $t < 25$ days after first light. This limit at 25 days is roughly when the recombination of hydrogen becomes the principal physical mechanism responsible for the escape of the shock deposited energy (Bersten et al. 2011; Pumo & Zampieri 2011; Pumo & Cosentino 2025). We then refer to spectra taken at more than 25 days past first-light as photospheric spectra. There are 40 SNe in the sample with early spectra, 18 of which show a featureless continuum, while 22 have measurable spectral features (that will be described in Section 3.6). Within the early spectra, there is a subset taken less than six days after first light, this subset is particularly interesting because it is in the range where the flash features are often produced (Bruch et al. 2021; Jacobson-Galán et al. 2024). We show this subset in Figure 3, and we analyze it in Section 3.6.

In our sample, we also have 45 SNe with photospheric spectra. Since we are interested in comparing photospheric properties with spectral measurements, especially of the Balmer features, we create a sub-sample of SNe to achieve this purpose.

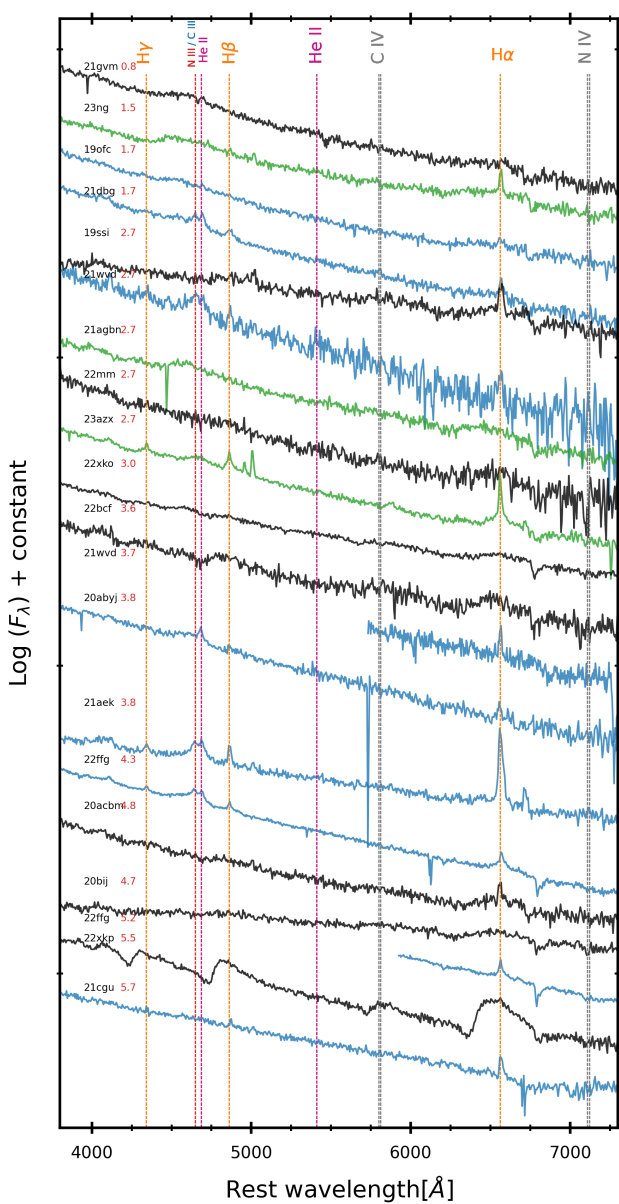


Fig. 3: Spectra of the sample taken within 6 days past first light. Marked with vertical dashed lines are the main emission lines in the early phase. Lines in gray mark typical flash emission features that we do not observe in our spectra. Non-flash SNe are marked with black, flash SNe with blue, and ledgers with green (see Section 3.6). The colour scheme is kept for the rest of the paper.

We collected all SNe that have photospheric spectra, with the requirement that they also have a measurable $H\beta$ profile. We define “measurable” when the $H\beta$ absorption is strong enough to be able to fit a low order polynomial to the minimum. Twenty one SNe II fulfill this criterion. For these SNe, we measured the expansion velocities of $H\alpha$, $H\beta$, and $Fe\ II\ \lambda 5169$ by fitting a low order polynomial to the minimum of the absorption profiles. The absorption minimum is often considered a reliable indicator of the bulk velocity of the material producing that line. An example of the minimum fit can be seen in Figure 4.

We relate the fastest material of the ejecta with the bluest wavelength of an absorption feature. We are interested in this in-

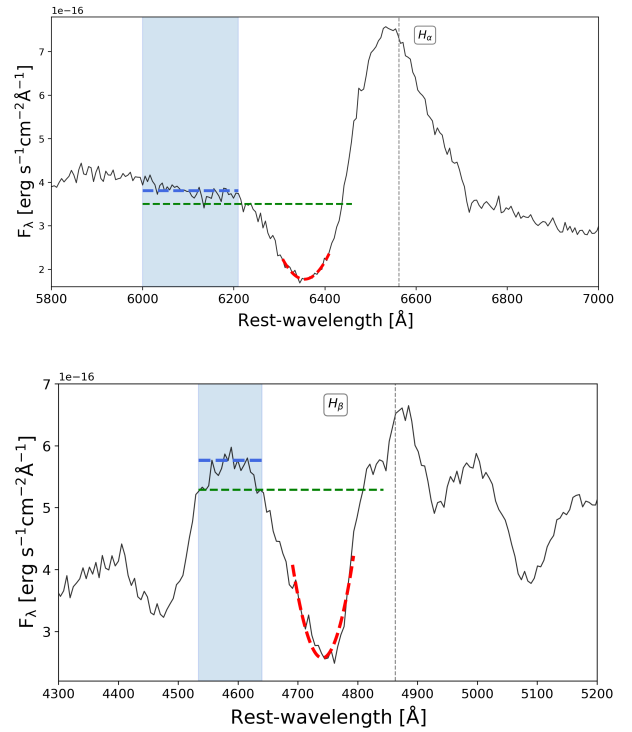


Fig. 4: Example of the fits and measurements of the minimum and the bluest wavelength for $H\alpha$ (top) and $H\beta$ (bottom). Marked in blue dashed lines are the fits to the pseudo-continuum to the blue side of $H\alpha$ (top), and on the feature next to $H\beta$ (bottom). The fits to the absorption minimum are marked in red for both panels, while the green line represents the value of the flux for which we consider the bluest wavelength of the feature.

formation because if significant CSM material exists in SNe II, then it will dampen this fastest material as the kinetic energy is converted into luminosity. Our method to measure this bluest wavelength was to define a pseudo-continuum level blueward of the absorption feature and then estimate the bluest extent of the absorption with respect to this defined continuum. We thus defined the bluest wavelength as the wavelength where the flux is lower than the continuum level by 15% of the maximum absorption. The 15% level was decided as a compromise between attempting to measure as close to the continuum level as possible and avoiding the typical noise fluctuation of our spectra. For $H\alpha$ measurements, we defined the level of the continuum by fitting a straight line in the range of 6000–6200 Å. $H\beta$ has other features to the blue and there is no smooth pseudo-continuum. Therefore, we took the emission to the left of the absorption, fitted a low order polynomial to that feature and took its maximum value as the level of the continuum. An example of these techniques is shown in Figure 4. Most of the uncertainty in the velocities was estimated by considering the standard deviation of repeated measurements when slightly changing the bluest and reddest wavelengths for the measurements.

Across our sample, we observe significant diversity in the $H\alpha$ profiles, both in the shape and the strength of the emission and absorption components. Gutiérrez et al. (2014) quantified this diversity by measuring the ratio of the equivalent widths (EWs) of the absorption to emission (a/e) components of $H\alpha$. Following their approach, we calculated this ratio by determining the EW of each component individually.

3.6. Classification of SNe II with high ionization lines

As described in Section 3.5, we obtained spectra for 18 SNe within the first six days post-first light (see Figure 3) and for five other SNe between six and ten days post-first light. Examining these early spectra, we observed that while some SNe appear featureless, others display narrow He II $\lambda 4686$ with electron-scattering broadened wings emission lines. This feature has been used in the literature to classify SNe II with “flash ionization” features (Khazov et al. 2016; Jacobson-Galán et al. 2024), assumed to be caused by interaction between the ejecta and the CSM. One of the primary goals of this work is to determine the frequency of CSM interaction and its impact on LCs and spectra at late times, making the identification of SNe with early interaction crucial. To achieve this, we classified SNe as either showing high-ionization features (“flash SNe”) or lacking them (“non-flash SNe”). With this purpose, we searched the Weizmann Interactive Supernova Data Repository (WISEREP⁷) for public spectra of SNe II, to augment our sample with the earliest spectra available. This search yielded 28 SNe with publicly available spectra.

Our sample includes 51 SNe with early spectra, combining our observations and public data. Of these, 42 SNe have spectra from 0 to 6 days after first light, while nine other have spectra from 6 to 10 days after first light. We classified them as flash or non-flash SNe by looking the profile of He II $\lambda 4686$. Although this line is present in all SNe II spectra, when it is Doppler-broadened and blue-shifted it forms in fast moving material, but when it is narrow with electron-scattering broadened wings it forms in unshocked CSM. Only in the latter case this line is an unambiguous signature of interaction. Thus to classify the SNe as flash, we look for narrow He II $\lambda 4686$ with electron-scattering broadened wings in its early spectra. To optimise objectivity, the authors KE, GF, and JA did this blindly, and discussed the results. The authors independently identified 18 SNe with high-ionization emission lines, including N III and He II. Additionally, we identified eight SNe displaying a broad emission feature around 4500–4800 Å with an irregular profile, referred to in the literature as a “ledge” feature, which has also been claimed to be associated with interaction (Bullivant et al. 2018; Andrews et al. 2019; Soumagnac et al. 2020). These SNe were classified as ledge cases. The remaining 25 SNe showed no flash features and were categorized as non-flash. In total, our sample consists of 18 flash SNe, eight ledge SNe, and 25 non-flash SNe. The classification for each SN as well as the references for the public spectra are listed in Table A.2. Additionally, an example of flash, non-flash, and ledge SNe is shown in Figure 5.

The origin of the ledge feature remains ambiguous, as will be discussed in Sections 4 and 5. Given the ongoing debate about whether this feature indicates interaction, we consider the SNe classified as ledgers both as SNe with signs of interaction and non-interaction in different analyses throughout the paper, to then compare our results under each assumption.

We identify two primary sources of uncertainty in our classifications: 1) classifying SNe using spectra obtained after 6 days post-first light to search for flash features may not be reliable, and 2) some spectra (approximately 4) have low signal-to-noise, which could hinder our ability to determine if there is possible excess emission. To address these issues, we defined one sub-sample consisting of 38 SNe classified as flash or non-flash SNe with high signal-to-noise (above 15 according to Bruch et al. 2021) spectra taken within 0 to 6 days post-first light, and an

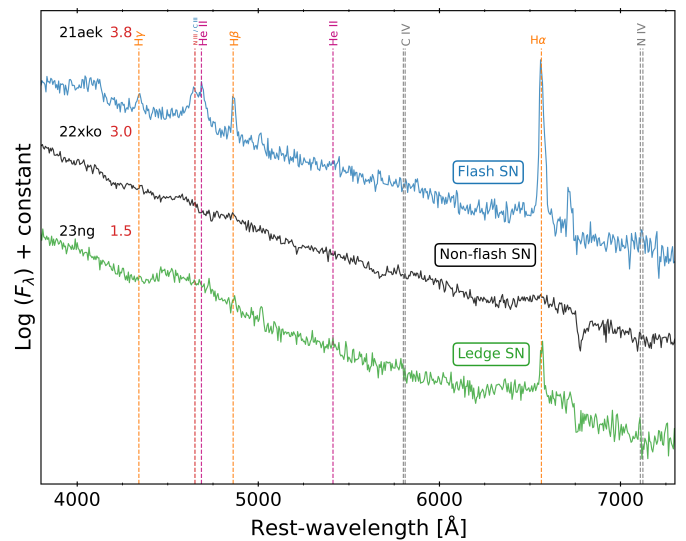


Fig. 5: An example of a flash (blue), non-flash (black), and ledge (green) SN. Vertical lines mark the main emission lines during the early phase.

other sub-sample including the remaining 13 SNe classified with spectra taken from 6 to 10 days post-first light and low signal-to-noise.

4. Results

4.1. Light-curve property distributions

The distributions of rise times, absolute magnitudes and decline rates for both ATLAS bands are shown in Figure 6. SN 1987A-like events are not included in this figure (nor subsequent ones), nor in presented distributions means, medians, etc.

The mean rise time of the sample in the o band is 11.8 days ($\sigma = 7.1$ days, 64 SNe), while the median is 9.1 days; in the c band the mean rise time is 10.7 ($\sigma = 7.7$ days, 21 SNe) and the median 7.7 days. The two longest rise times correspond to SN 2020vef and SN 2022iek, with values in the o band of 38.8 and 31.8 days, respectively; while the shortest rise times correspond to SN 2021sqg and SN 2020abyj with o band values of 1.9 and 2.2 days, respectively. The four 87A-like events, SN 2021aatd, SN 2021adcw, SN 2021adyl, and SN 2022acrv have rise times of 86.3, 52.9, 56.2, and 24.8 days, respectively. Note that SN 2021aatd and SN 2022acrv present additional early peaks in the LC, with initial rise times of 12.8 and 3.2 days, respectively.

Although there is no calculation of rise times in the literature for the ATLAS bands, in Table A.3 we compare our results with those of previous works that employed different bands. The o filter is roughly equivalent to $r + i$ filters, so it is suitable to compare our results with those previously calculated in the R/r bands. Our results are in agreement with those of González-Gaitán et al. (2015) for wavelengths > 7000 Å, but are somewhat higher than those calculated by Gall et al. (2015) and Rubin et al. (2016) and smaller than that calculated by Pessi et al. (2019). Although the dispersion in the literature values is high, our results are in agreement overall. The differences could be due to the fact that we are using a very broad filter. Note that, similar to González-Gaitán et al. (2015), we identify a subset of the sample with long rise times (i.e. longer than 15 d). We will discuss this issue in detail in Section 5.1.

⁷ <https://www.wiserep.org/>

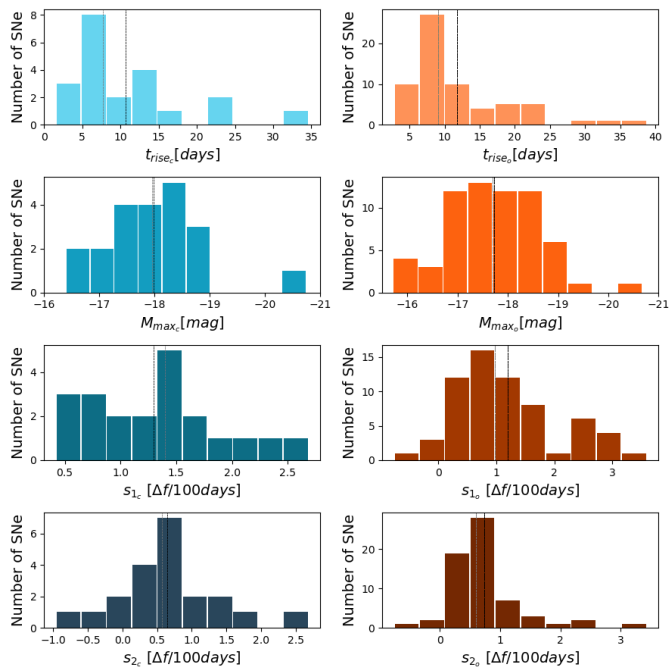


Fig. 6: Distribution of rise times, absolute magnitudes at maximum light, and decline rates for the SNe in the sample. Vertical dashed lines in black and gray indicate the mean and median of each distribution, respectively. This figure does not contain the 87A-like events. Left panel: ATLAS *c*-band. Right panel: ATLAS *o*-band

Focusing on the absolute magnitude distributions, the mean is -17.7 mag ($\sigma = 0.9$ mag, 64 SNe) and the median is -17.7 mag in the *o* band; in the *c* band the mean is -18.0 mag ($\sigma = 0.9$ mag, 21 SNe) and the median is -18.0 mag. In Table A.3 we compare our absolute peak magnitudes with those previously presented in the literature. There is no study to date that made these estimations for the ATLAS bands, so a direct comparison is not possible. However, the absolute magnitudes at maximum light we inferred are consistent within the dispersion, although slightly brighter than previous values available in the literature. The most luminous events in our sample are SN 2020znl and SN 2022yjl, while the dimmest are SN 2022xkp, SN 2022acko, and SN 2022acug. The bright events should be taken with caution because their distances may be not reliable. SN 2020znl exploded in the galaxy PS1-88920933245169840, which has no reported distance estimation. We also could not extract the H II region from its spectra (to enable an accurate redshift estimate), so we estimated its redshift by spectral matching with SNID, as stated in Section 3.2. Although its distance is not reliable, SN 2020znl does present a spectrum typical of luminous SNe II, with lack of H α absorption (Pessi et al. 2023). SN 2022yjl is an even more difficult case since it does not have an identified galaxy, and we could not get any spectrum to extract the H II region. We used the photo redshift value from its classification report (Li et al. 2022a). We lack a photospheric spectrum of SN 2022yjl to search for further evidence of high luminosity.

The mean s_1 is $1.2 \Delta f/100$ days ($\sigma = 0.9 \Delta f/100$ days, 64 SNe) in the *o* band and $1.3 \Delta f/100$ days ($\sigma = 0.6 \Delta f/100$ days, 21 SNe) in the *c* band. For s_2 , the mean is $0.7 \Delta f/100$ days for both the *o* band ($\sigma = 0.6 \Delta f/100$ days, 64 SNe) and the *c* band ($\sigma = 0.7 \Delta f/100$ days, 21 SNe). There are some objects in our sample that have large decline rates. These are SN 2020znl,

SN 2023cr, SN 2023dr, and SN 2023azx. It is worth noting all these SNe are either flash or ledgers. We will discuss this further in Section 4.3. We do not compare our decline rates with previous studies because, to maintain consistency throughout the paper, we express them in Δ flux per 100 days rather than magnitudes, preventing direct comparisons.

Two of the four SNe that show double-peaked LCs are 1987A-like events, so they were not included in the distributions, while the other two SNe were included. Although these last two may have a different behaviour compared to the rest of the sample, we leave them in the distributions since they are confirmed type II SNe. However, we note that all their parameters are calculated with respect to their first peak.

4.2. Spectral distributions

We focus our study of SN II spectral features by investigating the properties of H α , H β , and Fe II $\lambda 5169$. As an example, we show the H α bulk and bluest velocity evolutions in Figure 7.

H α shows a wide range of bulk velocities: from 5000 to 11000 km s^{-1} during early phases and from 6000 to 9500 km s^{-1} for most SNe in the photospheric phase. This is similar to what was obtained by Gutiérrez et al. (2017b), with H α expansion velocities ranging from 9500 to 1500 km s^{-1} at 50 days. For both H α and H β the lowest values of bulk velocities are those of SN 2020aze and SN 2020vef. For H β also SN 2022acmt is in the range of low values, but it is not present in the H α plot since it does not present an absorption component of H α . We could not measure the Fe II $\lambda 5169$ velocity for SN 2020aze and SN 2020vef since the feature was very weak.

When looking at the bluest velocities, SN 2020aze and SN 2022acmt appear well within the the rest of the distribution, while SN 2020vef remains with an extreme value. Other properties of these three SNe are: SN 2020aze shows the "Cachito" component in H α , also it is a part of the SNe with long rise times. SN 2020vef has a very weak H α absorption, and it also has a long time.

4.3. Correlations

Correlations between photometric parameters in the *o*-band, distinguishing flash SNe, non-flash SNe, and ledgers, are presented in Figure 8, as well as the cumulative distribution functions of the parameters. Table 2 provides the mean values for all photometric parameters for flash and non-flash SNe, with ledgers considered as part of each group separately. The table includes results for both the clean and unclean samples. Additionally, Table 3 shows the results of Anderson-Darling (A-D) tests for different groups across all parameters.

Flash and non-flash SNe exhibit significantly different mean s_1 decline rates, as illustrated in the upper panel of Figure 8. The ledger SNe appear to be spread across both groups. As seen in Table 3, an A-D test reveals a statistically significant difference in s_1 between the flash and non flash SNe. When including SNe classified as flash or non-flash based on spectra obtained 6–10 days after first light and low S/N ratios, the p-value remains statistically significant. These results suggest that SNe exhibiting high-ionization lines in their early spectra decline faster than those without signs of interaction. If the ledger SNe are considered as part of the flash SNe, the difference between the two populations becomes less pronounced but remains significant. However, it stays almost the same when treating ledgers as non-flash SNe. This suggests that ledgers present a distribution of s_1

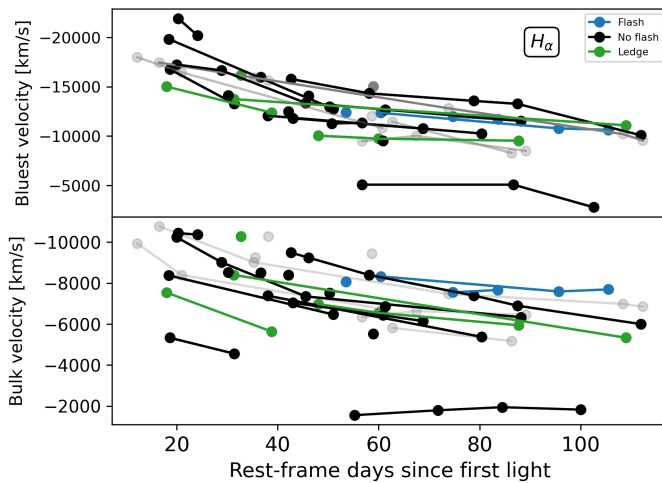


Fig. 7: $H\alpha$ bulk (upper panel) and bluest (lower panel) velocity evolution. Non-flash SNe are marked with black, flash SNe with blue, ledgers with green, and SNe without early spectra for flash classification are marked with gray. The errors are plotted but generally fall inside the data points.

Table 2: Mean values of the photometric parameters for the subsamples of flash and non-flash SNe. SNe classified as ledgers are included in both distributions separately. N is the number of SNe in each case.

SN II sample with spectra within 6 days of first light					
Classification	M_{max}	t_{rise}	s_1	s_2	N
Only flash SNe	-18.2 ± 0.5	10.0 ± 5.0	1.8 ± 0.8	0.7 ± 0.4	16
Only non-flash SNe	-17.3 ± 0.6	11.1 ± 4.2	0.7 ± 0.3	0.5 ± 0.3	14
Flash \cup ledgers	-17.8 ± 0.8	10.7 ± 6.0	1.5 ± 1.0	0.6 ± 0.4	23
Non – flash \cup ledgers	-17.2 ± 0.7	11.4 ± 5.6	0.7 ± 0.6	0.4 ± 0.3	21
SN II sample with spectra within 10 days of first light					
Only flash SNe	-18.2 ± 0.4	12.0 ± 7.5	1.7 ± 0.8	0.7 ± 0.4	18
Only non-flash SNe	-17.4 ± 0.7	12.6 ± 7.4	0.8 ± 0.6	0.8 ± 0.8	21
Flash \cup ledgers	-17.6 ± 0.8	11.9 ± 7.4	1.5 ± 1.0	0.6 ± 0.4	26
Non – flash \cup ledgers	-17.3 ± 0.8	12.3 ± 7.3	0.8 ± 0.7	0.6 ± 0.7	29

decline rates that is more similar to non-flash SNe than to flash SNe. On the other hand, we do not find different mean s_2 decline rates between flash and non-flash SNe.

Flash SNe are also systematically brighter than non-flash SNe in terms of M_{max} . For the SNe II sample with spectra within 6 days of first light, a A-D test returns a p-value of 0.001, demonstrating a significant difference. This trend persists when extending the analysis to include the SNe II with spectra within 10 days of first light. The difference also remains when ledger SNe are added, except in the case where they are considered as flash SNe in the 10-day sample, which weakens the distinction.

In contrast to decline rates and M_{max} , no significant difference is found in t_{rise} between flash and non-flash SNe. A-D tests for both the 6-day and 10-day samples consistently yield p-values greater than 0.2, suggesting no evidence for distinct populations based on this parameter.

We performed a Pearson test for the t_{rise} vs s_1 , t_{rise} vs M_{max} , and M_{max} vs s_1 and found correlation coefficients of -0.22, -0.14, and -0.56, respectively. Among these, the only strong correlation identified was between M_{max} and s_1 . No significant correlation was found between t_{rise} vs M_{max} or t_{rise} against the s_1 decline rate (see Section 5.1).

Figure 9 shows the evolution of the a/e ratio. SNe with the smallest a/e ratios correspond to those displaying high-ionization lines in their early-time spectra due to CSM interaction. Once

again, the ledgers SNe appear to be grouped with the non-flash population.

We studied the $H\alpha$, $H\beta$, and Fe II $\lambda 5169$ bulk and bluest velocities against absolute magnitude, decline rates, and rise times, respectively. In some SNe, the $H\beta$ feature was present and measurable, whereas $H\alpha$ was either absent or had an unmeasurable bluest wavelength. We calculated the Pearson correlation coefficients for the velocities against all the photometric parameters and found moderate correlations for the known relation of bulk velocity of $H\alpha$, $H\beta$, and Fe II $\lambda 5169$ vs absolute magnitude. Among these, Fe II $\lambda 5169$ exhibited the strongest and clearest correlation. No correlations were observed with the other photometric parameters.

5. Discussion

5.1. The rise times of SNe II

For an isolated star with no interaction with CSM, standard stellar evolution theory predicts that the rise to maximum light is primarily influenced by the radius of the progenitor star (Swartz et al. 1991; Gall et al. 2015). Larger progenitor radii result in SNe with longer rise times. Metallicity, indirectly, also plays a role, as it affects the pre-SN structure of the progenitor star (Chieffi et al. 2003; Tominaga et al. 2011). Specifically, lower metallicity leads to smaller radii, thereby impacting the rise times. However, González-Gaitán et al. (2015) found typical rise times of less than 10 days. When compared with analytical models, they found progenitor radii that were, on average, significantly smaller than those measured for observed RSG, suggesting that the rise times are too short to be explained by an isolated star with no CSM. Supporting this finding, Förster et al. (2018) reported a steep rise lasting just a few days in their sample of SNe II. By comparing these observations to models, they inferred high CSM densities for most events and concluded that this likely reflects the systematic detection of shock breakouts within a dense CSM.

The relatively short rise times motivated modelling efforts of SNe II with CSM interaction. Morozova et al. (2017) first modelled three well-studied Type II events, finding that these were well-reproduced by RSG surrounded by dense CSM. The extent of the CSM and the wind velocity suggested that these stars likely experienced enhanced mass-loss activity during the last months to years of their lives. Then, Moriya et al. (2023) demonstrated that the rise times of SNe II are predominantly influenced by the properties of the CSM, such as its radius, mass, and mass-loss rate, as well as the explosion energy. According to Moriya et al. (2018), when the mass loss rate is sufficiently high ($\dot{M} > 10^{-3} M_{\odot} \text{ yr}^{-1}$), the rise times are primarily governed by the mass-loss rates. Interestingly, the rise times initially decrease as \dot{M} increases, but beyond a certain threshold, they begin to lengthen with further increases in \dot{M} .

Our results are broadly consistent with these previous studies, since the majority of SNe II in our sample exhibit short rise times. While the mean rise time in the o -band for our sample is 11.7 days, there is a fraction of SNe – without taking into account 87A-like events – with longer rise times (longer than 15 days⁸). These are 16 SNe, representing $\approx 24\%$ of the sample. Figure 8 shows that SNe with long rise times seem to have slow declines and also tend to be brighter. Regarding their velocities, it has been proposed that SNe II with long rise times and high

⁸ The choice of this value is arbitrary and it is based on the number adopted by González-Gaitán et al. (2015) to separate SNe with short and long rise times.

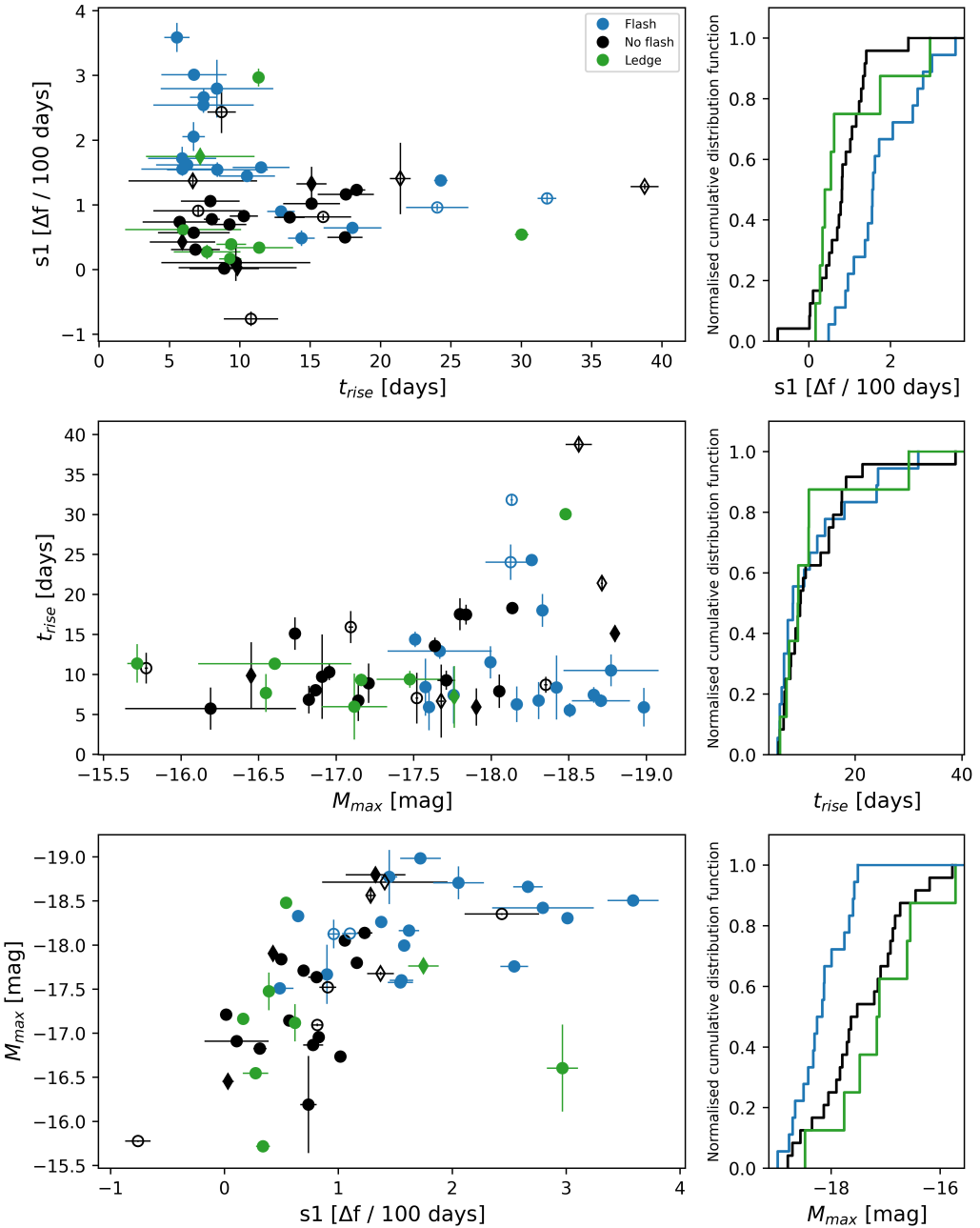


Fig. 8: Correlations between photometric parameters in the sample. Non-flash SNe are marked with black, while flash SNe are marked with blue. Ledgers are marked with green and SNe without early spectra for flash classification are marked with gray. Filled circles indicate SNe classified as flash or non-flash based on spectra obtained within six days of first light and with high signal-to-noise. Diamond symbols represent classifications based on low signal-to-noise spectra, while open symbols correspond to SNe classified with spectra taken between 6 and 10 days after first light.

Table 3: Results of the A-D tests for different groups. For each parameter and each group the A^2 statistic is listed, along with the p-value. Highlighted in bold are those p-values < 0.05 .

SN II sample with spectra within 6 days of first light				
Classification	M_{max}	t_{rise}	s_1	s_2
Flash vs Non-flash SNe	7.601/ 0.001	-0.178/0.250	8.846/ 0.001	0.863/0.145
Flash \cup ledgers vs Non-flash SNe	2.855/ 0.02	-0.480/0.250	3.703/ 0.001	-0.416/0.25
Flash SNe vs Non – flash \cup ledgers	9.843/ 0.001	0.086/0.250	10.084/ 0.001	2.859/ 0.022
SN II sample with spectra within 10 days of first light				
Flash SNe vs Non-flash SNe	8.786/ 0.001	-0.374/0.250	8.227/ 0.001	0.148/0.250
Flash \cup ledgers vs Non-flash SNe	1.554/0.074	-0.577/0.250	3.708/ 0.01	-0.190/0.250
Flash SNe vs Non – flash \cup ledgers	8.035/ 0.001	-0.341/0.250	8.262/ 0.001	1.305/0.094

$\text{H}\alpha$ velocities may be a link between type IIs and IIBs (Davis et al. 2021). Although we do not have spectra for all the SNe with long rise times, those SNe that have show $\text{H}\alpha$ velocities consistent with other normal type II SN samples (Gutiérrez et al. 2017a).

Previously, González-Gaitán et al. (2015) identified a fraction of SNe in their sample with long rise times. Although classified as Type IIs based on photometry, these events lacked spectroscopic confirmation. Those authors suggested that these SNe might originate from a different progenitor system and argued that this provides strong evidence that typical SNe II are limited to short rise times, while other possible hydrogen-rich SNe may exhibit longer rise times. In contrast, all SNe with long rise times in our sample are spectroscopically confirmed as normal Type II.

When taking into account the early classification as flash or non flash SNe, we find that 4 of the SNe with long rise times are flash SNe, 8 are non-flash SNe, 1 is a ledger and for three of them, we do not have early spectra to classify. Although modelling the progenitor properties of these SNe is beyond the scope of this paper, we can speculate on possible scenarios. For SNe with long rise times and no signs of CSM interaction, it is plausible that they originate from standard RSGs without surrounding CSM, consistent with predictions from standard stellar evolution theory. On the other hand, for SNe displaying early spectral evidence of interaction, the findings of Moriya et al. (2018) may provide a natural explanation in which sufficiently high, but not extreme, mass-loss rates can lead to extended rise times without producing SNe powered by interaction, as seen in SNe IIn.

Overall, our rise time distributions show that SNe with early spectral signatures of CSM interaction are not confined to either the short or long ends of the rise times range but are rather spread across the distribution. This could be due, as commented before, to the multiple factors that affect the rise times.

5.2. Links between early-time and late time SN II properties

We find that flash SNe exhibit faster decline rates in s_1 and are brighter than those without signs of interaction. This result contrasts with previous studies, such as that of Bruch et al. (2023), who reported no significant differences in brightness, colour, or rise times between SNe II with and without flash ionization features. In addition, Bruch et al. (2023) found no differences in magnitudes, redshift, or the epoch of the first spectrum between flash and non-flash SNe, indicating that selection effects did not influence their results. We examined these same properties in our sample and likewise found no significant differences. The discrepancy between the two studies may therefore arise from differences in sample size (only 17 events in Bruch et al. 2023 work), or in the treatment of SNe showing the ledge or Doppler-broadened He II profiles, which they treat as flash SNe.

Despite this tension, recent studies report trends consistent with our findings. For example, Jacobson-Galán et al. (2025) found that flash SNe have significantly higher luminosities and decline rates at +50 days than non-flash SNe, while Jiang et al. (2025) reported higher post-peak decline rates for SNe with larger CSM masses. Together, these results support our conclusion that CSM properties influence not only the early-time spectra but also the overall LC evolution. More specifically, the differences between flash and non-flash SNe II with respect to decline rates appear to be confined to the early s_1 decline - i.e. that from peak to the start of the plateau. This suggests that the presence and diversity of this initial decline rate may be dominated by the extent and profile of CSM above the progenitor density profile.

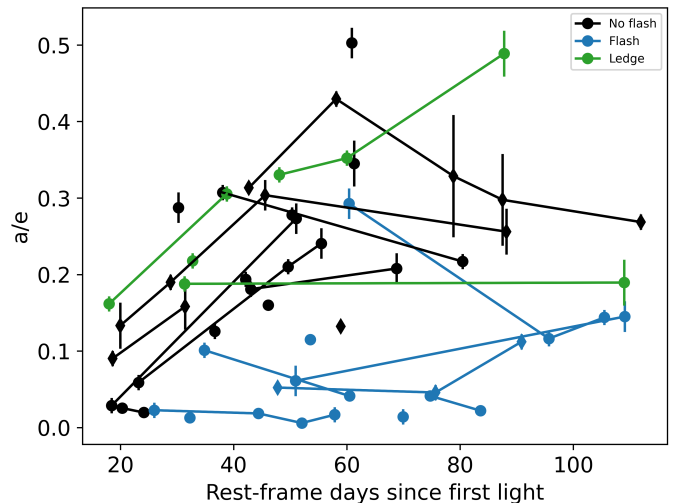


Fig. 9: Evolution of the a/e ratio. Non-flash SNe are marked with black, flash SNe with blue, and ledgers with green.

An interesting finding of this work is the evolution of the a/e ratio, as shown in Figure 9. Our analysis reveals a distinct division: SNe that exhibit high-ionization lines in their early spectra tend to have smaller a/e ratios compared to those without such features. This ratio, which accounts for the diversity in the $\text{H}\alpha$ absorption profile, has been previously studied by several authors. To explain the absence or weakening of the absorption component, Schlegel (1996) proposed three plausible scenarios. First, the absorption component could be filled in by additional emission produced via scattering, potentially originating from CSM or a highly extended SN envelope. Second, it could be a low mass envelope which would have less matter to absorb, and no P-Cygni profile will be formed. Lastly, a steep density gradient in the hydrogen envelope could reduce the amount of absorbing material at high velocities, leading to the suppression of P-Cygni absorption. Additionally, Gutiérrez et al. (2014) analysed the a/e ratio in a large sample of SNe II and concluded that variations in the $\text{H}\alpha$ P-Cygni profile are most likely associated with changes in the envelope properties (such as its mass and density profile) and the degree of CSM interaction. Furthermore, Gutiérrez et al. (2014) found that SNe with smaller a/e have more rapidly declining LCs and are brighter at maximum light. Consistent with these findings, our results show that SNe with signs of interaction in the early spectra tend to be brighter, have rapidly declining LCs, and have the lowest a/e ratios, indicating a lack or depletion of $\text{H}\alpha$ absorption. This aligns with the predictions of Schlegel (1996) and Gutiérrez et al. (2014), reinforcing the role of CSM interaction in shaping the observed profiles.

One matter of debate in this work is the association of ledge SNe with the other groups, not only in the a/e ratio evolution but also within the distribution of parameters. They appear to group with the non-flash population. Ledge features have been observed in early spectra several times in the literature (e.g. Quimby et al. 2007; Shivers et al. 2015; Bullivant et al. 2018), either alone or blended with a narrow component of high-ionization lines. However, its origin remains a subject of debate. One explanation is that the ledge arises from a very broad, blueshifted He II $\lambda 4686$ line, formed from the SN ejecta beneath a CSM shell (Bullivant et al. 2018; Andrews et al. 2019), although when this solution was proposed, there was a narrow

component of this line present. This interpretation, however, is hard to reconcile with the irregular profile of the feature. Alternatively, the ledge might result from a blend of several high-ionization lines of C, N, and O originating in the CSM (Soumagnac et al. 2020; Bruch et al. 2021). However, this hypothesis is complicated by the feature’s width, as these high-ionization lines would need to be significantly broader or more numerous to explain the observed profile. Hosseinzadeh et al. (2022) offered another possibility, suggesting that the explosion of an RSG with an extended envelope into a low-density CSM could produce the ledge-shaped feature without generating the high-ionization lines typically associated with flash ionization. The closer association of ledger SNe with the non-flash group would suggest that the origin of the ledge feature may be different from that of the flash features.

6. Conclusions

In this work we have presented a sample of 68 SNe II with early-time photometric observations from the ATLAS survey and complementary spectroscopy from the ePESSTO+ collaboration. By combining well-constrained light curves with early and photospheric spectra, we investigated the impact of CSM interaction on the photometric and spectroscopic evolution of SNe II.

We identified early-time high-ionization, electron-scattered broadened spectral features—a sign of CSM interaction—in 18 SNe (flash SNe), and contrasted their properties with those of 25 non-flash SNe. An additional subset of 8 SNe displayed the ambiguous “ledge” feature, and we evaluated their properties under both the flash and non-flash assumptions to test their association.

Our main findings are as follows:

- Flash SNe exhibit significantly faster s_1 decline rates and higher peak luminosities compared to non-flash SNe. This suggests that early interaction with CSM not only affects spectral features but also alters the energy release observed in the light curves. However, no significant difference in rise time was found between flash and non-flash SNe, maybe suggesting that rise times alone are not a reliable diagnostic for early interaction.
- A clear distinction in the $H\alpha$ a/e ratio was observed between the two groups. Flash SNe consistently show lower a/e values at all epochs, which may reflect suppression of absorption due to enhanced CSM interaction or altered density structures in the outer ejecta.
- SNe displaying the ledge feature tend to align more closely with the non-flash population in terms of decline rates, peak brightness, and a/e ratios. While the origin of this feature remains uncertain, our results suggest that these events may represent a lower level or different manifestation of interaction, distinct from that seen in flash SNe.
- A subset of SNe II in our sample, without considering the 87A-like events, exhibits long rise times (>15 days). These include both flash and non-flash SNe, suggesting multiple physical origins. Some may arise from extended progenitor envelopes or dense CSM capable of delaying shock breakout, while others may reflect standard RSG explosions with minimal surrounding material.

This work shows the value of combining early-time photometric and spectroscopic observations to characterise the diversity of SNe II and the frequency and impact of early CSM interaction. Future high-cadence surveys with rapid spectroscopic follow-up will be key to improving our understanding of the final

stages of massive star evolution and the role of CSM in shaping SN observables.

Acknowledgements. This work has made use of data from the Asteroid Terrestrial-impact Last Alert System (ATLAS) project. The Asteroid Terrestrial-impact Last Alert System (ATLAS) project is primarily funded to search for near earth asteroids through NASA grants NN12AR55G, 80NSSC18K0284, and 80NSSC18K1575; byproducts of the NEO search include images and catalogs from the survey area. This work was partially funded by Kepler/K2 grant J1944/80NSSC19K0112 and HST GO-15889, and STFC grants ST/T000198/1 and ST/S006109/1. The ATLAS science products have been made possible through the contributions of the University of Hawaii Institute for Astronomy, the Queen’s University Belfast, the Space Telescope Science Institute, the South African Astronomical Observatory, and The Millennium Institute of Astrophysics (MAS), Chile. Based on observations collected at the European Southern Observatory under the ePESSTO+ programmes with ID: 106.216C, 108.220C, and 1103.D-0328 (PI: Inserra). CPG acknowledges financial support from the Secretary of Universities and Research (Government of Catalonia) and by the Horizon 2020 Research and Innovation Programme of the European Union under the Marie Skłodowska-Curie and the Beatriu de Pinós 2021 BP 00168 programme, from the Spanish Ministerio de Ciencia e Innovación (MCIN) and the Agencia Estatal de Investigación (AEI) 10.13039/501100011033 under the PID2023-151307NB-I00 SNNEXT project, from Centro Superior de Investigaciones Científicas (CSIC) under the PIE project 20215AT016 and the program Unidad de Excelencia María de Maeztu CEX2020-001058-M, and from the Departament de Recerca i Universitats de la Generalitat de Catalunya through the 2021-SGR-01270 grant. AA acknowledges the Yushan Young Fellow Program by the Ministry of Education, Taiwan, for the financial support (MOE-111-YSFMS-0008-001-P1). T.-W.C. acknowledges the financial support from the Yushan Fellow Program by the Ministry of Education, Taiwan (MOE-111-YSFMS-0008-001-P1) and the National Science and Technology Council, Taiwan (NSTC grant 114-2112-M-008-021-MY3). TP and EC acknowledges the financial support from the Slovenian Research Agency (grants I0-0033, P1-0031, J1-8136, J1-2460 and the Young researchers program). L.G. acknowledges financial support from AGAUR, CSIC, MCIN and AEI 10.13039/501100011033 under projects PID2023-151307NB-I00, PIE 20215AT016, CEX2020-001058-M, ILINK23001, COOPB2304, and 2021-SGR-01270. T.E.M.B. is funded by Horizon Europe ERC grant no. 101125877.

References

Anderson, J. P., González-Gaitán, S., Hamuy, M., et al. 2014, ApJ, 786, 67
 Andrews, J. E., Sand, D. J., Valenti, S., et al. 2019, ApJ, 885, 43
 Bazin, G., Palanque-Delabrouille, N., Rich, J., et al. 2009, A&A, 499, 653
 Beasor, E. R. & Davies, B. 2018, MNRAS, 475, 55
 Bersten, M. C., Benvenuto, O., & Hamuy, M. 2011, ApJ, 729, 61
 Blondin, S. & Tonry, J. L. 2007, ApJ, 666, 1024
 Bruch, R. J., Gal-Yam, A., Schulze, S., et al. 2021, ApJ, 912, 46
 Bruch, R. J., Gal-Yam, A., Yaron, O., et al. 2023, ApJ, 952, 119
 Bullivant, C., Smith, N., Williams, G. G., et al. 2018, MNRAS, 476, 1497
 Burke, J., Hiramatsu, D., Howell, D. A., et al. 2021, Transient Name Server Classification Report, 2021-3199, 1
 Buzzoni, B., Delabre, B., Dekker, H., et al. 1984, The Messenger, 38, 9
 Chieffi, A., Domínguez, I., Höflich, P., Limongi, M., & Straniero, O. 2003, MNRAS, 345, 111
 Cosentino, S. P., Pumo, M. L., & Cherubini, S. 2025, MNRAS, 540, 2894
 Dahiwale, A. & Fremling, C. 2020, Transient Name Server Classification Report, 2020-3138, 1
 Das, K. K., Kasliwal, M. M., Sollerman, J., et al. 2025, arXiv e-prints, arXiv:2506.20068
 Davis, S., Pessi, P. J., Fraser, M., et al. 2021, ApJ, 909, 145
 de Jaeger, T., Anderson, J. P., Galbany, L., et al. 2018, MNRAS, 476, 4592
 Dessart, L., Hillier, D. J., & Audit, E. 2017, A&A, 605, A83
 Dessart, L. & Jacobson-Galán, W. V. 2023, A&A, 677, A105
 Dimitriadis, G., Foley, R. J., Terreran, G., & Angus, C. R. 2021, Transient Name Server AstroNote, 184, 1
 Do, A., Tucker, M. A., Payne, A. V., et al. 2020, Transient Name Server Classification Report, 2020-1479, 1
 Domínguez, A., Siana, B., Henry, A. L., et al. 2013, ApJ, 763, 145
 Faran, T., Poznanski, D., Filippenko, A. V., et al. 2014, MNRAS, 442, 844
 Fitzpatrick, E. L. 1999, PASP, 111, 63
 Foreman-Mackey, D., Hogg, D. W., Lang, D., & Goodman, J. 2013, PASP, 125, 306
 Förster, F., Moriya, T. J., Maureira, J. C., et al. 2018, Nature Astronomy, 2, 808
 Fraser, M., Maund, J. R., Smartt, S. J., et al. 2012, ApJ, 759, L13
 Fremling, C., Sharma, Y., & Dahiwale, A. 2019, Transient Name Server Classification Report, 2019-1808, 1

Fulton, M., Srivastav, S., Smartt, S. J., et al. 2022, Transient Name Server Classification Report, 2022-911, 1

Gall, E. E. E., Polshaw, J., Kotak, R., et al. 2015, *A&A*, 582, A3

González-Gaitán, S., Tominaga, N., Molina, J., et al. 2015, *MNRAS*, 451, 2212

Gutiérrez, C. P., Anderson, J. P., Hamuy, M., et al. 2014, *ApJ*, 786, L15

Gutiérrez, C. P., Anderson, J. P., Hamuy, M., et al. 2017a, *ApJ*, 850, 90

Gutiérrez, C. P., Anderson, J. P., Hamuy, M., et al. 2017b, *ApJ*, 850, 89

Hinkle, J. 2022a, Transient Name Server Classification Report, 2022-1342, 1

Hinkle, J. 2022b, Transient Name Server Classification Report, 2022-3327, 1

Hinkle, J. 2023, Transient Name Server Classification Report, 2023-54, 1

Hosseinzadeh, G., Kilpatrick, C. D., Dong, Y., et al. 2022, *ApJ*, 935, 31

Itagaki, K. 2023, Transient Name Server Discovery Report, 2023-1158, 1

Jacobson-Galán, W. V., Dessart, L., Davis, K. W., et al. 2025, *ApJ*, 992, 100

Jacobson-Galán, W. V., Dessart, L., Davis, K. W., et al. 2024, *ApJ*, 970, 189

Jiang, N., Moon, D.-S., Ni, Y. Q., et al. 2025, *ApJ*, 989, 53

Khazov, D., Yaron, O., Gal-Yam, A., et al. 2016, *ApJ*, 818, 3

Kilpatrick, C. D., Foley, R. J., Jacobson-Galán, W. V., et al. 2023, *ApJ*, 952, L23

Leonard, D. C., Filippenko, A. V., Barth, A. J., & Matheson, T. 2000, *ApJ*, 536, 239

Li, L., Zhai, Q., Zhang, J., & Wang, X. 2022a, Transient Name Server Classification Report, 2022-3099, 1

Li, L., Zhai, Q., Zhang, J., & Wang, X. 2022b, Transient Name Server Classification Report, 2022-3605, 1

Li, L., Zhai, Q., Zhang, J., & Wang, X. 2022c, Transient Name Server Classification Report, 2022-106, 1

Li, W., Leaman, J., Chornock, R., et al. 2011, *MNRAS*, 412, 1441

Lin, H., Zhang, J., Wang, X., et al. 2025, *MNRAS*, 540, 2591

Maund, J. R., Smartt, S. J., & Danziger, I. J. 2005, *MNRAS*, 364, L33

Moriya, T., Tominaga, N., Blinnikov, S. I., Baklanov, P. V., & Sorokina, E. I. 2011, *MNRAS*, 415, 199

Moriya, T. J., Förster, F., Yoon, S.-C., Gräfener, G., & Blinnikov, S. I. 2018, *MNRAS*, 476, 2840

Moriya, T. J., Subrayan, B. M., Milisavljevic, D., & Blinnikov, S. I. 2023, *PASJ*, 75, 634

Morozova, V., Piro, A. L., & Valenti, S. 2017, *ApJ*, 838, 28

Nagao, T., Pastorello, A., & Reguitti, A. 2022, Transient Name Server Classification Report, 2022-2910, 1

Niemela, V. S., Ruiz, M. T., & Phillips, M. M. 1985, *ApJ*, 289, 52

Ochner, P., Benetti, S., Tomasella, L., et al. 2022, Transient Name Server AstroNote, 18, 1

Olivares E., F., Hamuy, M., Pignata, G., et al. 2010, *ApJ*, 715, 833

Payne, A. V. 2022, Transient Name Server Classification Report, 2022-728, 1

Pellegrino, C., Farah, J., Howell, D. A., et al. 2023, Transient Name Server Classification Report, 2023-218, 1

Pessi, P. J., Anderson, J. P., Folatelli, G., et al. 2023, *MNRAS*, 523, 5315

Pessi, P. J., Folatelli, G., Anderson, J. P., et al. 2019, *MNRAS*, 488, 4239

Phillips, M. M., Simon, J. D., Morrell, N., et al. 2013, *ApJ*, 779, 38

Planck Collaboration, Aghanim, N., Akrami, Y., et al. 2020, *A&A*, 641, A6

Poznanski, D., Ganeshalingam, M., Silverman, J. M., & Filippenko, A. V. 2011, *MNRAS*, 415, L81

Pumo, M. L. & Cosentino, S. P. 2025, *MNRAS*, 538, 223

Pumo, M. L. & Zampieri, L. 2011, *ApJ*, 741, 41

Quimby, R. M., Wheeler, J. C., Höflich, P., et al. 2007, *ApJ*, 666, 1093

Rodríguez, Ó., Clochiciatti, A., & Hamuy, M. 2014, *AJ*, 148, 107

Rodríguez, Ó., Maoz, D., & Nakar, E. 2023, *ApJ*, 955, 71

Rodríguez, Ó., Meza, N., Pineda-García, J., & Ramirez, M. 2021, *MNRAS*, 505, 1742

Rodríguez, Ó., Pignata, G., Hamuy, M., et al. 2019, *MNRAS*, 483, 5459

Rubin, A., Gal-Yam, A., De Cia, A., et al. 2016, *ApJ*, 820, 33

Schlafly, E. F. & Finkbeiner, D. P. 2011, *ApJ*, 737, 103

Schlegel, D. J., Finkbeiner, D. P., & Davis, M. 1998, *ApJ*, 500, 525

Schlegel, E. M. 1990, *MNRAS*, 244, 269

Schlegel, E. M. 1996, *AJ*, 111, 1660

Shivvers, I., Groh, J. H., Mauerhan, J. C., et al. 2015, *ApJ*, 806, 213

Shivvers, I., Modjaz, M., Zheng, W., et al. 2017, *PASP*, 129, 054201

Smartt, S. J. 2015, *PASA*, 32, e016

Smartt, S. J., Valenti, S., Fraser, M., et al. 2015, *A&A*, 579, A40

Smith, K. W., Smartt, S. J., Young, D. R., et al. 2020, *PASP*, 132, 085002

Smith, K. W., Srivastav, S., Smartt, S. J., et al. 2021, Transient Name Server AstroNote, 235, 1

Sonnett, S., Meech, K., Jedicke, R., et al. 2013, *PASP*, 125, 456

Soumagnac, M. T., Ganot, N., Irani, I., et al. 2020, *ApJ*, 902, 6

Srivastav, S., Chen, T. W., Smartt, S. J., et al. 2024, Transient Name Server AstroNote, 100, 1

Srivastav, S., Smartt, S. J., Fulton, M., et al. 2021, Transient Name Server Classification Report, 2021-2493, 1

Srivastav, S., Smartt, S. J., McBrien, O., et al. 2020, Transient Name Server Classification Report, 2020-2884, 1

Swartz, D. A., Wheeler, J. C., & Harkness, R. P. 1991, *ApJ*, 374, 266

Taguchi, K., Kawabata, M., & Maeda, K. 2022, Transient Name Server Classification Report, 2022-3326, 1

Tammann, G. A. & Schroeder, A. 1990, *A&A*, 236, 149

Terreran, G., Li, W., Arcavi, I., Lam, M., & Keinan, I. 2022, Transient Name Server Classification Report, 2022-3582, 1

Tominaga, N., Morokuma, T., Blinnikov, S. I., et al. 2011, *ApJS*, 193, 20

Tonry, J. L. 2011, *PASP*, 123, 58

Tonry, J. L., Denneau, L., Heinze, A. N., et al. 2018, *PASP*, 130, 064505

Turatto, M., Benetti, S., & Cappellaro, E. 2003, in From Twilight to Highlight: The Physics of Supernovae, ed. W. Hillebrandt & B. Leibundgut, 200

Van Dyk, S. D., Cenko, S. B., Poznanski, D., et al. 2012, *ApJ*, 756, 131

Yaron, O., Perley, D. A., Gal-Yam, A., et al. 2017, *Nature Physics*, 13, 510

¹ Facultad de Ciencias Astronómicas y Geofísicas, Universidad Nacional de La Plata, Paseo del Bosque S/N, B1900FWA, La Plata, Argentina

e-mail: keilaertini@gmail.com

² Instituto de Astrofísica de La Plata (IAP), CCT-CONICET-UNLP, Paseo del Bosque S/N, B1900FWA, La Plata, Argentina

³ European Southern Observatory, Alonso de Córdova 3107, Casilla 19, Santiago, Chile

⁴ Kavli Institute for the Physics and Mathematics of the Universe (WPI), The University of Tokyo Institutes for Advanced Study, The University of Tokyo, Kashiwa, 277-8583 Chiba, Japan

⁵ Instituto de Astrofísica e Ciências do Espaço, Faculdade de Ciências, Universidade de Lisboa, Ed. C8, Campo Grande, 1749-016 Lisbon, Portugal

⁶ Institut d'Estudis Espacials de Catalunya (IEEC), Edifici RDIT, Campus UPC, 08860 Castelldefels (Barcelona), Spain

⁷ Institute of Space Sciences (ICE, CSIC), Campus UAB, Carrer de Can Magrans, s/n, E-08193 Barcelona, Spain

⁸ The Oskar Klein Centre, Department of Astronomy, Stockholm University, Albanova University Center, SE 106 91 Stockholm, Sweden

⁹ Pontificia Universidad Católica de Chile, Vicuña Mackenna 4860, Macul, Santiago, Chile

¹⁰ Instituto Milenio de Astrofísica (MAS), Nuncio Monseñor Sótero Sanz 100, Of. 104, Santiago, Chile

¹¹ Graduate Institute of Astronomy, National Central University, 300 Jhongda Road, 32001 Jhongli, Taiwan

¹² Center for Astrophysics and Cosmology, University of Nova Gorica, Vipavska 11c, 5270 Ajdovščina, Slovenia

¹³ University of Catania, Department of Physics and Astronomy "E. Majorana", Italy

¹⁴ Institut d'Astrophysique de Paris (IAP), Sorbonne Université, CNRS, Paris, France

¹⁵ South African Astronomical Observatory, Cape Town, 7925, South Africa

¹⁶ Department of Physics, Stellenbosch University, Stellenbosch, 7602, South Africa

¹⁷ School of Physics, University College Dublin, LMI Main Building, Beech Hill Road, Dublin 4, Ireland

¹⁸ Astronomical Observatory, University of Warsaw, Al. Ujazdowskie 4, 00-478 Warszawa, Poland

¹⁹ Cardiff Hub for Astrophysics Research and Technology, School of Physics & Astronomy, Cardiff University, Queens Buildings, The Parade, Cardiff, CF24 3AA, UK

²⁰ School of Physics, Trinity College Dublin, The University of Dublin, Dublin 2, Ireland

²¹ Instituto de Ciencias Exactas y Naturales (ICEN), Universidad Arturo Prat, Chile

²² Astrophysics Division, National Centre for Nuclear Research, Pasteura 7, 02-093 Warsaw, Poland

²³ Instituto de Alta Investigación, Universidad de Tarapacá, Casilla 7D, Arica, Chile

²⁴ Dipartimento di Fisica "Ettore Pancini", Università di Napoli Federico II, Via Cinthia 9, 80126 Naples, Italy

²⁵ INAF - Osservatorio Astronomico di Capodimonte, Via Moiariello 16, I-80131 Naples, Italy

²⁶ Astrophysics sub-Department, Department of Physics, University of Oxford, Keble Road, Oxford, OX1 3RH, UK

²⁷ Astrophysics Research Centre, School of Mathematics and Physics, Queen's University Belfast, Belfast BT7 1NN, UK

Appendix A: Properties of the sample

Table A.1: SN II Sample

SN	Host Galaxy	z	$E(B - V)_{MW}$	Last non-det	Discovery Date	Exp epoch
SN 2019ofc	LCRS B013124.4-385126	0.020	0.01	58715.63	58717.51	58716.57
SN 2019pnl	LEDA 997304	0.040	0.07	58726.56	58730.55	58728.55
SN 2019ssi	UGC 12640	0.013	0.06	58773.38	58775.37	58774.37
SN 2019uhm	WISEA J102849.18-312953.3	0.010	0.05	58789.64	58791.64	58790.64
SN 2019vjl	NGC 3015	0.025	0.07	58802.64	58808.62	58805.63
SN 2019xtw	ESO299-G013	0.016	0.01	58837.34	58839.27	58838.30
SN 2020aze	NGC 3318	0.009	0.06	58871.50	58875.47	58873.48
SN 2020bij	NGC 3463	0.013	0.06	58875.56	58877.51	58876.53
SN 2020szs	CGCG 402-005	0.022	0.03	59102.39	59103.40	59102.90
SN 2020vef	SDSS J034211.73-002113.0	0.026	0.06	59130.52	59132.49	59131.51
SN 2020voh	6dFJ230350.8-360124 (LARS)	0.016	0.001	59129.38	59131.37	59130.37
SN 2020xoq	2MASX J20030114-4133024	0.031	0.08	59137.24	59139.22	59138.23
SN 2020znl	PS1 88920933245169840	0.037	0.23	59160.54	59164.51	59162.52
SN 2020abyj	ESO476-G023	0.032	0.01	59189.32	59191.29	59190.31
SN 2020acbm	LSBC F831-08	0.022	0.02	59192.40	59194.35	59193.38
SN 2021aek	I SZ 091	0.022	0.04	59223.59	59227.57	59225.58
SN 2021cgu	CGCG 038-099	0.025	0.03	59248.57	59252.52	59250.54
SN 2021dbg	S4YI000212 (GSC cat)	0.020	0.02	59256.44	59260.42	59258.43
SN 2021gvm	SDSS J132959.99+132446.0	0.023	0.02	59293.50	59297.42	59295.46
SN 2021mqh	MCG -01-30-021	0.021	0.03	59350.39	59352.31	59351.35
SN 2021qvr	NGC 7678	0.011	0.04	59383.57	59387.60	59385.58
SN 2021rem	2MASX J15194792+1341104	0.029	0.03	59391.36	59392.38	59391.87
SN 2021tiq	MCG -02-57-024	0.023	0.05	59408.51	59412.51	59410.51
SN 2021tyw	UGC 12354	0.013	0.20	59417.62	59419.50	59418.56
SN 2021tsz	SDSS J233758.38-002629.6	0.040	0.03	59412.57	59414.51	59413.54
SN 2021sqg	ESO287-G018	0.015	0.02	59399.62	59403.46	59401.54
SN 2021wvd	CGCG077-028	0.045	0.03	59449.31	59451.27	59450.29
SN 2021yyg	2MASX J05162092-1328164	0.011	0.13	59470.62	59471.59	59471.11
SN 2021wyn	2MASS J00411206-1442024	0.053	0.02	59445.46	59447.45	59446.46
SN 2021aatd	GALEXASC J005904.40-001210.0	0.015	0.02	59492.51	59494.37	59493.44
SN 2021adcw	2MASS J02043283-2107094	0.018	0.01	59519.49	59523.44	59521.46
SN 2021afkk	UGC 01971	0.015	0.09	59541.42	59543.37	59542.39
SN 2021agbn	2MASX 03571315-2523551	0.014	0.03	59547.43	59551.36	59549.40
SN 2021adyl	IC2479	0.028	0.02	59523.61	59525.58	59524.59
SN 2021yja	NGC1325	0.005	0.01	59463.48	59465.55	59464.51
SN 2022bcf	MCG -01-12-043	0.016	0.10	59608.84	59610.24	59609.54
SN 2022jo	IC 4040	0.025	0.009	59587.62	59589.46	59588.54
SN 2022mm	UGCA258	0.013	0.04	59588.57	59590.64	59589.60
SN 2022abq	NGC 5117	0.008	0.01	59597.55	59601.59	59599.57
SN 2022big	ORPHAN	0.018	0.017	59604.88	59606.87	59605.88
SN 2022fqe	NGC 5995	0.025	0.14	59669.06	59670.53	59669.79
SN 2022etp	2MASX J14221000+2505490	0.038	0.01	59649.49	59651.48	59650.49
SN 2022kad	CGCG076-118	0.019	0.03	59712.51	59716.49	59714.50
SN 2022jdf	SDSS J151828.21+051422.0	0.035	0.04	59699.22	59700.40	59699.81
SN 2022iek	UGC05818	0.021	0.02	59691.12	59692.33	59691.73
SN 2022ibv	ESO437-G064	0.014	0.05	59690.15	59690.87	59690.51
SN 2022frq	MCG -02-34-054	0.022	0.05	59670.43	59672.92	59671.68
SN 2022fli	HIDEEP J1342-3405	0.025	0.04	59661.33	59665.90	59664.12
SN 2022jox	ESO 435- G 014	0.008	0.09	59706.04	59709.02	59707.53
SN 2022ffg	CGCG 093-074	0.012	0.035	59663.35	59664.30	59663.83
SN 2022rje	GALEXASCJ045753.84-161502.7	0.021	0.076	59806.62	59807.39	59807.01
SN 2022yjl	SDSS J221758.36+105943.4	0.080	0.059	59872.82	59874.34	59873.58
SN 2022xkp	LCRS B025030.8-412847	0.012	0.016	59860.18	59862.28	59861.73
SN 2022xko	ESO 014- G 001	0.015	0.076	59861.98	59864.27	59863.12
SN 2022wsp	NGC7448	0.007	0.04	59854.40	59855.13	59854.77
SN 2022zkc	GIN227	0.032	0.04	59884.03	59885.20	59884.62
SN 2022aagp	NGC 2777	0.005	0.038	59894.57	59897.55	59896.06

Table A.1 - (continued)

SN	Host Galaxy	z	$E(B - V)_{MW}$	Last non-det	Discovery Date	Exp epoch
SN 2022aacn	LEDA 5807554	0.018	0.031	59895.43	59896.39	59895.91
SN 2022acmt	ESO547-G027	0.033	0.03	59921.18	59922.14	59921.66
SN 2022acko	2MASXiJ0319359-192344	0.006	0.02	59918.17	59919.92	59919.04
SN 2022acug	S5XX016714 (GSC cat)	0.010	0.078	59921.91	59924.15	59923.03
SN 2022acyd	SDSS J040111.13+053305.7	0.035	0.237	59927.16	59928.69	59927.93
SN 2022acrv	PS1 83820866869460987	0.034	0.045	59921.27	59922.25	59921.76
SN 2023cr	ESO419-G003	0.014	0.011	59950.90	59951.83	59951.36
SN 2023dr	VIII Zw 154	0.035	0.042	59951.29	59952.97	59952.13
SN 2023ng	2MASX J091522.0-185217	0.017	0.058	59957.25	59958.29	59957.77
SN 2023aub	IC 4219	0.012	0.057	59969.37	59970.31	59969.84
SN 2023azx	PS1 88791808263516143	0.011	0.045	59971.32	59972.05	59971.69

Table A.2: SN II Sample spectral information

SN	N of spectra	Earliest and latest epoch	Classification	Reference for classification
SN 2019ofc	5	1.7 - 107	F	This work
SN 2019pnl	4	49.7 - 94.5	F	Fremling et al. (2019)
SN 2019ssi	3	2.7 - 51.7	NF	This work
SN 2019uhm	5	16.7 - 113.5	N/A	-
SN 2019vjl	5	10.7 - 98.5	N/A	-
SN 2019xtw	1	42.8	NF	Do et al. (2020)
SN 2020aze	4	7.7 - 31.7	NF	This work
SN 2020bij	2	4.7 - 46.7	NF	This work
SN 2020szs	1	60.2	NF	Srivastav et al. (2020)
SN 2020vef	6	56.7 - 116.6	NF	Dahiwale & Fremling (2020)
SN 2020voh	4	15.8 - 87.7	N/A	-
SN 2020xoq	2	9.8 - 23.9	NF	This work
SN 2020znl	9	11.6 - 85.6	N/A	-
SN 2020abyj	5	3.8 - 59.7	F	This work
SN 2020acbmm	4	4.8 - 56.7	NF	This work
SN 2021aek	9	3.8 - 61.8	F	This work
SN 2021cgu	3	5.7 - 106.5	F	This work
SN 2021dbg	3	1.7 - 54.6	F	This work
SN 2021gvm	3	0.8 - 24.7	NF	This work
SN 2021mqh	0	-	F	Jacobson-Galán et al. (2024)
SN 2021qvr	4	42.8 - 106.6	F	Jacobson-Galán et al. (2024)
SN 2021rem	0	-	NF	Dimitriadis et al. (2021)
SN 2021tiq	8	17.7 - 114.6	NF	Srivastav et al. (2021)
SN 2021tyw	18	6.7 - 110.5	F	This work
SN 2021tsz	1	14.8	N/A	-
SN 2021sqg	4	30.6 - 90.5	N/A	-
SN 2021wvd	4	2.7 - 9.7	F	This work
SN 2021yyg	7	12.3 - 89.2	NF	Burke et al. (2021)
SN 2021wyn	2	54.7	N/A	-
SN 2021aattd	3	8.8 - 30.8	NF	This work
SN 2021adew	3	21.8 - 59.7	N/A	-
SN 2021afkk	0	-	F	Jacobson-Galán et al. (2024)
SN 2021agbn	3	2.7 - 110.6	L	This work
SN 2021adyl	1	49.7	N/A	-
SN 2021yja	5	6.8 - 16.8	L	This work
SN 2022bcf	1	3.6	NF	This work
SN 2022jo	1	62.8	NF	Li et al. (2022c)
SN 2022mm	4	2.7 - 69.7	NF	This work
SN 2022abq	1	50.7	NF	Ochner et al. (2022)
SN 2022big	0	-	N/A	-
SN 2022fqe	0	-	NF	Fulton et al. (2022)
SN 2022etp	0	-	NF	Payne (2022)
SN 2022kad	0	-	NF	Hinkle (2022a)
SN 2022jdf	1	22.5	N/A	-
SN 2022iek	1	11.4	F	This work

Table A.2 - (continued)

SN	N of spectra	Earliest and latest epoch	Classification	Reference for classification
SN 2022ibv	0	-	F	Jacobson-Galán et al. (2024)
SN 2022frq	0	-	NF	Jacobson-Galán et al. (2024)
SN 2022fli	1	39.1	N/A	-
SN 2022jox	0	-	F	Jacobson-Galán et al. (2024)
SN 2022ffg	3	4.3 - 7.3	F	This work
SN 2022rje	1	36.3	N/A	-
SN 2022yjl	0	-	N/A	-
SN 2022xkp	3	5.5 - 81.4	NF	This work
SN 2022xko	2	3.0 - 37.2	NF	This work
SN 2022wsp	1	61.3	NF	Nagao et al. (2022)
SN 2022zkc	1	71.5	N/A	-
SN 2022aagp	4	48.3 - 88.2	L	Taguchi et al. (2022)
SN 2022aacn	0	-	NF	Hinkle (2022b)
SN 2022acmt	1	52.4	L	Terreran et al. (2022)
SN 2022acko	2	18.1 - 39.0	L	Lin et al. (2025)
SN 2022acug	3	12.3 - 61.3	N/A	-
SN 2022acyd	1	56.1	F	Li et al. (2022b)
SN 2022acrv	2	22.4 - 36.3	N/A	-
SN 2023cr	2	6.7 - 32.7	F	This work
SN 2023dr	0	-	F	Hinkle (2023)
SN 2023ng	2	1.5 - 33.3	L	This work
SN 2023aub	0	-	L	Pellegrino et al. (2023)
SN 2023azx	2	2.7 - 24.6	L	This work

Table A.3: LC properties compared with previous works in the literature. When available, the standard error of the mean is listed.

Reference	N of SNe	Wavelength [Å] / band	t _{rise} [days]	M _{max} [mag]
This work	64	<i>o</i>	11.8 ± 0.8	-17.7 ± 0.1
	21	<i>c</i>	10.7 ± 1.7	-18.0 ± 0.2
Tammann & Schroeder (1990)	23	<i>B</i>	-	-17.2 ± 0.3
Anderson et al. (2014)	116	<i>V</i>	-	-16.7 ± 0.1
Gutiérrez et al. (2014)	52	<i>V</i>		-16.7
González-Gaitán et al. (2015)	223	<4000	<10	-
	223	>7000	12-15	-
Gall et al. (2015)	20	<i>r'/R</i>	10.2 ± 0.2	-
Rubin et al. (2016)	57	<i>R</i>	7.7 ± 0.4	-
Gutiérrez et al. (2017b)	99	<i>V</i>	-	-16.7 ± 0.1
	73	<i>B</i>	8.3 ± 0.2	-
Pessi et al. (2019)	73	<i>V</i>	12.8 ± 0.3	-
	73	<i>r</i>	16 ± 0.4	-
Bruch et al. (2021)	17	<i>g</i>	8.9	-17.7
	16	<i>r</i>	12.7	-17.7
Rodríguez et al. (2021)	60	<i>R</i>	-	-16.7 ± 0.1
Das et al. (2025)	129	<i>r</i>	13 ^{+0.4} _{-0.2}	-

Appendix B: SNe light-curves with their fits

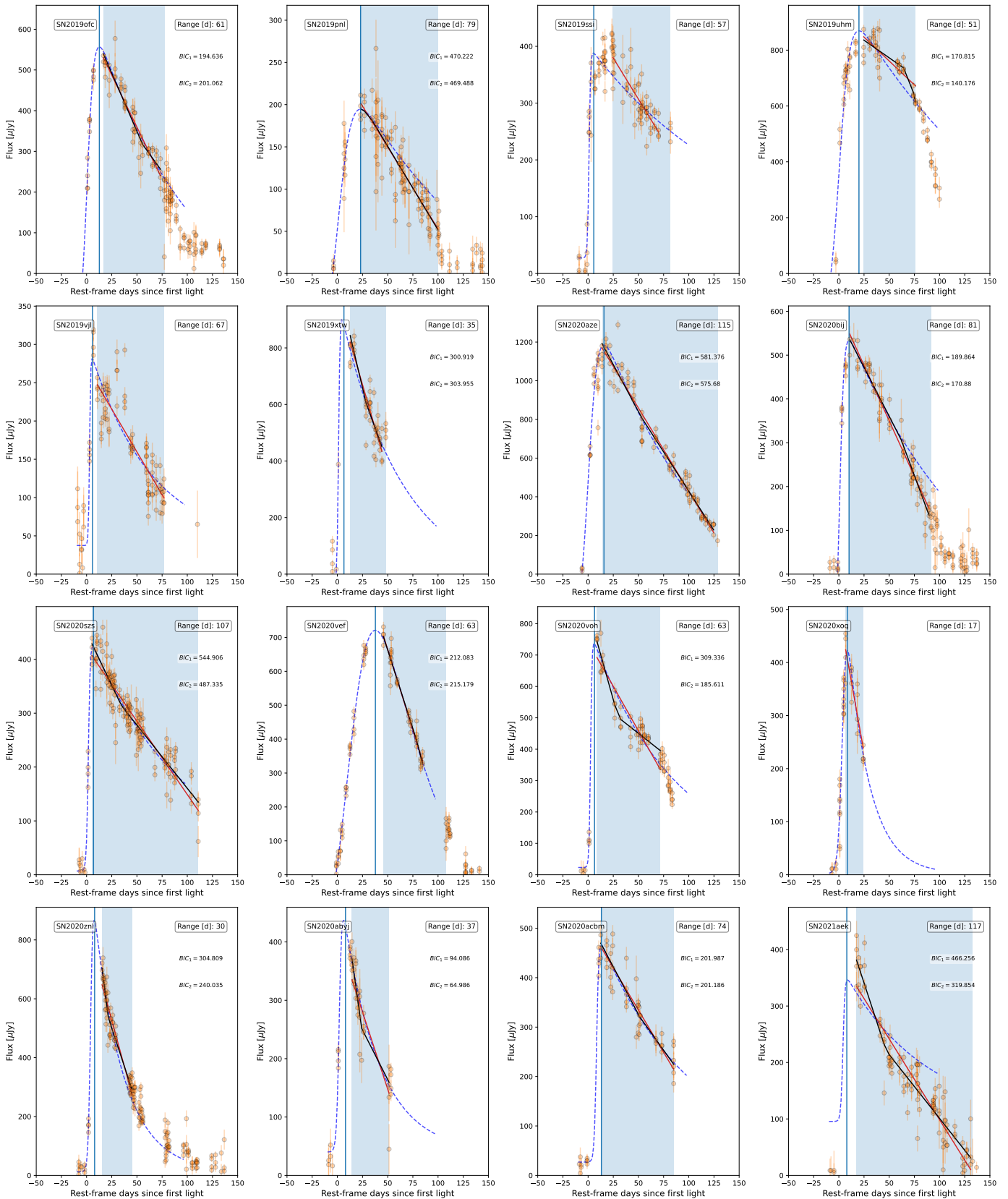


Fig. B.1: LCs of the SNe II from the sample in the o band shown in orange. Marked with dashed blue lines are the fits to the LCs. The time of maximum light is shown with vertical lines. The light blue bands mark the range where the fits to calculate the decline rates were made. Marked with red lines are the fits to the LCs with one slope and with black are the fits with two slopes. In those cases where the two slopes regime provided bad fits, only the fits with one slope are plotted.

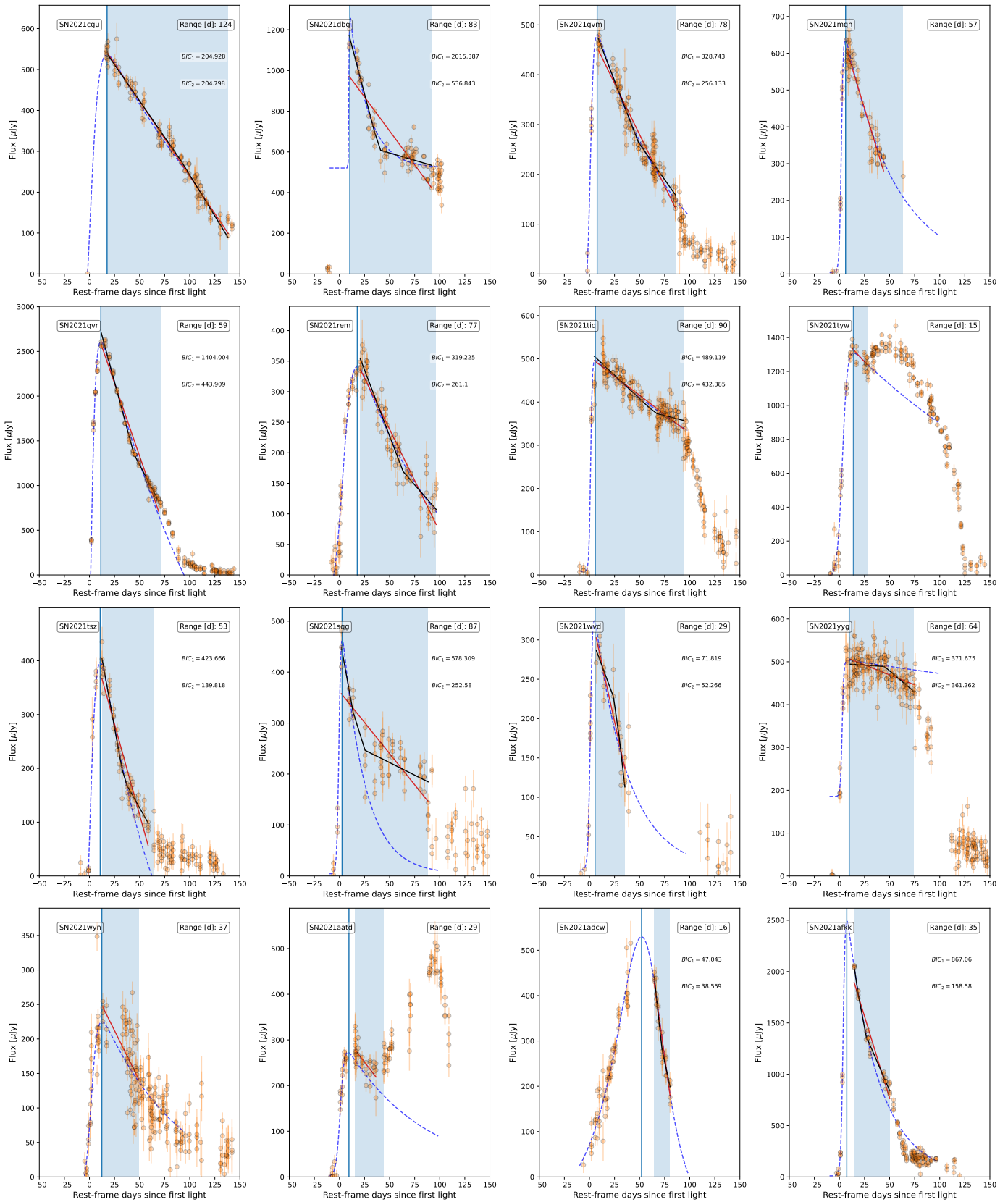


Fig. B.1: Continued.

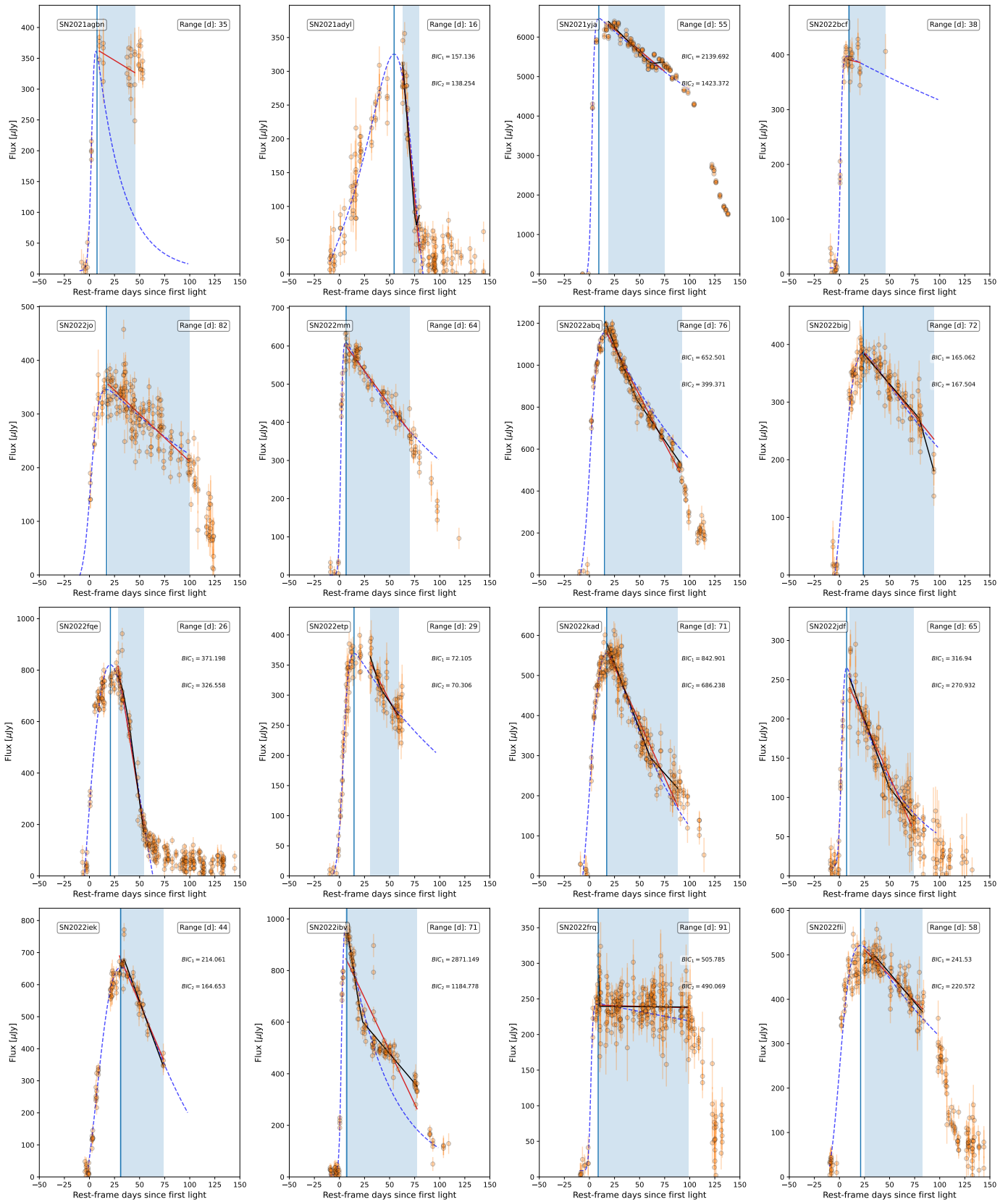


Fig. B.1: Continued.

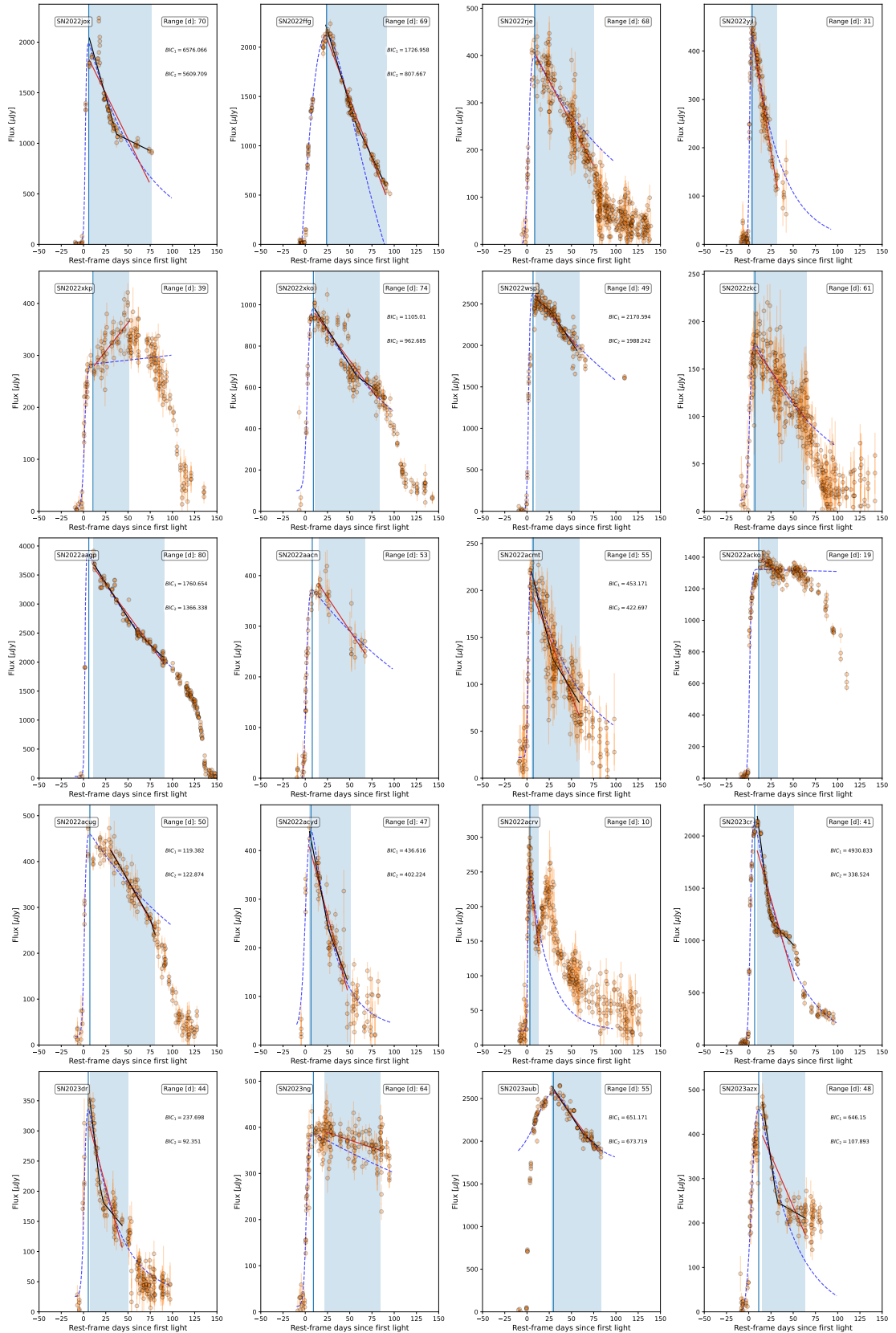


Fig. B.1: Continued.

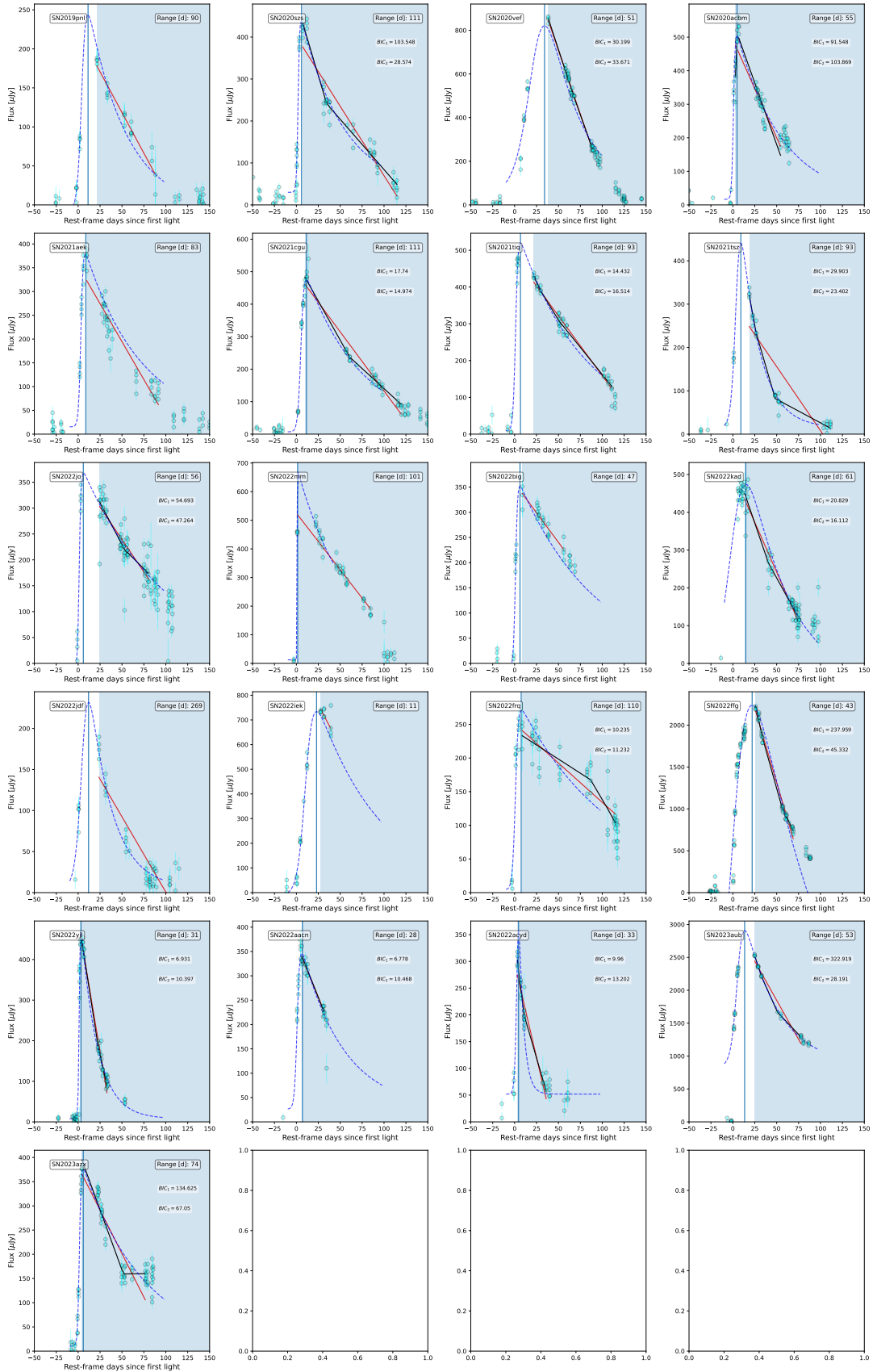


Fig. B.2: LCs of the SNe II from the sample in the c band shown in cyan. Marked with dashed bluelines are the fits to the LCs. The light blue bands mark the range where the fits to calculate the decline rates were made. Marked with red lines are the fits to the LCs with one slope and with black are the fits with two slopes. The time of maximum light is shown with vertical lines. In those cases where the two slopes regime provided bad fits, only the fits with one slope are plotted.